LAWRENCE
LIVERMORE
NATIONAL
LABORATORY

UCRL-JRNL-229505

Corrosion Resistance of Amorphous Fe49.7Cr17.7Mn1.9Mo7.4W1.6B15.2C3.8Si2. coating - a new criticality-controlled material

J.C. Farmer, J-S. Choi, C-K. Saw, R. Rebak, S.D. Day,
T. Lian, P. Hailey, J.H. Payer, D.J. Branagan, L.F.
Aprigliano

March 28, 2007

Journal of Nuclear Technology

Disclaimer

CORROSION RESISTANCE OF AMORPHOUS $Fe_{49.7}Cr_{17.7}Mn_{1.9}Mo_{7.4}W_{1.6}B_{15.2}C_{3.8}Si_{2.4}$ COATING – A NEW CRITICALITY-CONTROL MATERIAL

J. C. Farmer, J-S. Choi, C-K. Saw, R. H. Rebak, S. D. Day, T. Lian and P. D. Hailey
Lawrence Livermore National Laboratory, Livermore, California

J. H. Payer
Case Western Reserve University, Cleveland, Ohio

D. J. Branagan
The NanoSteel Company, Idaho Falls, Idaho

L. F. Aprigliano
Strategic Analysis, Arlington, Virginia

An iron-based amorphous metal with good corrosion resistance and a high absorption cross-section for thermal neutrons has been developed and is reported here. This amorphous alloy has the approximate formula $Fe_{49.7}Cr_{17.7}Mn_{1.9}Mo_{7.4}W_{1.6}B_{15.2}C_{3.8}Si_{2.4}$ and is known as SAM2X5. Chromium (Cr), molybdenum (Mo) and tungsten (W) were added to provide corrosion resistance, while boron (B) was added to promote glass formation and the absorption of thermal neutrons. Since this amorphous metal has a higher boron content than conventional borated stainless steels, it provides the nuclear engineer with design advantages for criticality control structures with enhanced safety. While melt-spun ribbons with limited practical applications were initially produced, large quantities (several tons) of gas atomized powder have now been produced on an industrial scale, and applied as thermal-spray coatings on prototypical half-scale spent nuclear fuel containers and neutron-absorbing baskets. These prototypes and other SAM2X5 samples have undergone a variety of corrosion testing, including both salt-fog and long-term immersion testing. Modes and rates of corrosion have been determined in various relevant environments, and are reported here. While these coatings have less corrosion resistance than melt-spun ribbons and optimized coatings produced in the laboratory, substantial corrosion resistance has been achieved.

I. INTRODUCTION

I.A. Historical Perspective

The outstanding corrosion resistance that may be possible with amorphous metals was recognized several years ago.[1-3] Compositions of several iron-based amorphous metals were published, including several with very good corrosion resistance. Examples include thermally sprayed coatings of Fe-10Cr-10-Mo-(C,B), and bulk Fe-Cr-Mo-C-B and Fe-Cr-Mo-C-B-P.[4-6] The corrosion resistance of an iron-based amorphous alloy with yttrium, $Fe_{48}Mo_{14}Cr_{15}Y_2C_{15}B_6$, was also established.[7-11] Yttrium was added to this alloy to lower the critical cooling rate. In addition to iron-based materials, nickel-based amorphous metals were also developed that exhibited exceptional corrosion performance in acids. Very good nickel-based crystalline coatings were deposited with thermal spray, but appeared to have less corrosion resistance than amorphous-metal coatings.[12]

I.B. Enhanced Corrosion Resistance

Several corrosion-resistant iron-based amorphous alloys have been developed that can be applied as thermal spray coatings. One of the most promising formulations is SAM2X5 ($Fe_{49.7}Cr_{17.7}Mn_{1.9}Mo_{7.4}W_{1.6}B_{15.2}C_{3.8}Si_{2.4}$), which includes relatively high concentrations of Cr, Mo, and W for enhanced corrosion resistance, and substantial B to enable glass formation and neutron absorption. This alloy was identified through the systematic exploration of composition, which involved adding 1, 3, 5, and 7 atomic percent Ni, Mo, Y, Ti, Zr or Cr to a common parent alloy known as SAM40. Specifically, SAM2X5 was made by adding 5 atomic-percent molybdenum to SAM40. The parent alloy is described in substantial detail in the patent literature.[13-14] The target compositions of this alloy, other amorphous alloys in the same family, and crystalline alloys such as Type 316L stainless steel (UNS # S31603) and nickel-based Alloy C-22 (UNS # N06022) are given in Table I.

Conclusions regarding the exceptional passive film stability and corrosion resistance of this iron-based amorphous alloy, compared to crystalline reference materials, were based on measurements of passive film breakdown potential and corrosion rate, as well as observed performance during salt fog testing. Such measurements enabled the corrosion performance of various iron-based amorphous alloys, carbon steel, iron-based stainless steels and nickel-based alloys to be directly compared.

It has been recognized that the corrosion resistance of both iron- and nickel based crystalline alloys can be enhanced through the additions of Cr, Mo and W for many years.[15-16] These alloying elements also enhance the corrosion resistance of iron-based amorphous metals. While the pitting resistance equivalence number was developed for crystalline alloys, it was used for guidance in determining maximum beneficial elemental concentrations of Cr, Mo and W used in the materials studied here. Initial calculations of the PREN for these amorphous alloys were done using formulae from the published literature.

As pointed out in the literature, an estimate of the relative pitting resistance of alloys can be made using the PREN, which is calculated using the elemental composition of the alloy.[17-21] PREN values for the Fe-based amorphous metals of interest here, and the crystalline reference materials, which include Type 316L stainless steel and Ni-based Alloy C-22, have been calculated using the following equations, and are presented in Table VIII. Equation 6 has been used for estimating the PREN for nickel-based alloys, and accounts for the beneficial effects of Cr, Mo, W and N on corrosion resistance: [17]

$$PREN = [\%Cr] + 3.3 \times [\%Mo + \%W] + 30 \times [\%N] \tag{1}$$

However, this equation was used to predict comparable corrosion resistance for Alloys C-276 and Alloy C-22, while Alloy C-22 was known to be more corrosion resistant. An equation that has been used to make reasonable predictions of the relative corrosion resistance of austenitic stainless steels and nickel-based alloys such as Alloy C-22 is: [18]

$$PREN = [\%Cr] + 3.3 \times \left([\%Mo] + 0.5 \times [\%W]\right) + k \times [\%N] \tag{2}$$

The factor k is an adjustable parameter used to account for the beneficial effects of nitrogen. Reasonable values of the factor k range from 12.8 to 30, with 16 being commonly accepted as a reasonable value by Sedriks and others.[19] Estimates presented here are based on the assumption that the value of k is 16.

PREN values calculated with Equation 7 indicated that the resistance of the SAM2X5 and SAM1651 amorphous metal formulations should be more resistant to localized corrosion than Type 316L stainless steel or nickel-based Alloy C-22. As in the case of crystalline Fe-based and Ni-based alloys, it was found experimentally that the addition of Cr, Mo, and W substantially increased the corrosion resistance of these amorphous alloys. Additional passive film stability may have been observed, which cannot be attributed to composition alone, and may be attributable to the glassy structure. Additional work is required to further understand the relative roles of composition and crystalline structure in high-performance amorphous metal coatings, such as the ones discussed here.

An obvious deficiency associated with the use of a parameter based on chemical composition alone to assess the relative corrosion resistance of both crystalline and amorphous alloys is that microstructural effects on passive film breakdown are ignored. The lack of crystalline structure is believed to be a key attribute of corrosion resistant amorphous metals.

The corrosion resistance of iron-based amorphous alloys such as SAM2X5 can be further enhanced by increasing the concentration of chromium, molybdenum, tungsten and other beneficial elements. The neutron absorption cross-section can be enhanced by increasing the concentration of boron, other neutron-absorbing elements, and different isotopes.

I.C. Good Thermal Stability

The thermal properties of these Fe-based amorphous metals have been previously determined and are summarized in Table II.[22] Thermal analysis of these Fe-based amorphous metals, using differential scanning calorimetry (DSC) or differential thermal analysis (DTA), allowed determination of important thermal properties such as the glass transition temperature (T_g), crystallization temperature (T_x), and the melting point (T_m). Results from the thermal analysis of amorphous samples provided initial assessment of the glass forming ability of these materials through conventional metrics, such as the reduced glass transition temperature ($T_{rg} = T_g/T_L$). As the Mo additions to SAM40 were increased from 1 to 7 atomic percent, T_x increased from ~620 to ~630°C, and T_m increased from 1110 to 1137°C. Other trends with composition were less obvious. The thermal properties for SAM2X5 are: $T_g \sim 579$°C; $T_x \sim 628$°C; $T_m \sim 1133$°C; and $T_{rg} \sim 0.51$. Similarly, the thermal properties for SAM2X7 are: $T_g \sim 573$°C; $T_x \sim 630$°C; $T_m \sim 1137$°C; and $T_{rg} \sim 0.50$. Typical critical cooling rates for these alloys are roughly 600 Kelvin per second.

I.D. High Hardness

Hardness determines wear resistance, as well as resistance to erosion-corrosion. Vickers micro-hardness (HV) was the standard approach used to assess the hardness of thermal-spray coatings.[22] A 300-gram load was used since it was believed that this load and the affected area were large enough to sample across any existing macro-porosity, thereby producing a spatially averaged measurement. Micro-hardness measurements were also made with a 100-gram load since it was believed that this load and the affected area were small enough to accurately sample bulk material properties. Micro-hardness measurements made with the 100-gram load were: 1050-1200 kg mm^{-2} (HVN) for as-sprayed high-velocity oxy-fuel (HVOF) coatings; and 1300-1500 kg mm^{-2} (HVN) for materials that were annealed 700°C for 10 minutes to induce devitrification. Micro-hardness measurements made with the 100-gram load were: 1050-1200 kg mm^{-2} (HVN) for as-sprayed HVOF coatings; and 1300-1500 kg mm^{-2} (HVN) for materials that were annealed 700°C for 10 minutes to induce devitrification. The increase in hardness with devitrification is attributed to the formation of crystalline precipitates.

I.E. Enhanced Criticality Safety

The high boron content of $Fe_{49.7}Cr_{17.7}Mn_{1.9}Mo_{7.4}W_{1.6}B_{15.2}C_{3.8}Si_{2.4}$ (SAM2X5) makes it an effective absorber of thermal neutrons, and suitable for criticality control applications. Such boron-containing amorphous metals may prove to be beneficial for the storage of spent nuclear fuel with enhanced criticality safety.[22-24] Measured values of the neutron absorption cross-section in transmission (Σ_t) for several materials of interest, including SAM2X5 HVOF coatings, are summarized in Table III. Average values for 316L, C-22, borated stainless steel, Ni-Cr-Mo-Gd, and SAM2X5 are 1.1, 1.3, 2.3, 3.8 and 7.1 cm^{-1} respectively.[24] The relatively high value for SAM2X5 provides clear insight into the potential importance of this new material to the nuclear industry. Given this potential application, it should be noted that this material and its parent alloy have also been shown to remain in the amorphous state after receiving relatively high neutron dose, and after annealing at temperatures up to the glass transition temperature.[24]

II. EXPERIMENTAL

II.A. Melt Spinning Process

Maximum cooling rates of one million Kelvin per second (10^6 K/s) have been achieved with melt spinning, which is an ideal process for producing amorphous metals over a very broad range of compositions. This process was used to synthesize completely amorphous, Fe-based, corrosion-resistant alloys with near theoretical density, and thereby enabled the effects of coating morphology on corrosion resistance to be separated from the effects of elemental composition. The melt-spun ribbon (MSR) samples prepared with this equipment were several meters long, several millimeters wide and approximately 150 microns thick.

II.B. Thermal Spray Process

The coatings discussed here were made with the HVOF process, which involves a combustion flame, and is characterized by gas and particle velocities that are three to four times the speed of sound. This process is ideal for depositing metal and cermet coatings, which have typical bond strengths of 34-69 MPa (nominally 5,000 to 10,000 pounds per square inch), porosities of less than one percent (< 1%) and extreme hardness. The cooling rate that can be achieved in a typical thermal spray process such as HVOF are on the order of ten thousand Kelvin per second (10^4 K/s), and are high enough to enable many alloy compositions to be deposited above their respective critical cooling rate (CCR), thereby maintaining the vitreous state. However, the range of amorphous metal compositions that can be processed with HVOF is more restricted than those that can be prepared with melt spinning, due to the differences in achievable cooling rates. Both kerosene and hydrogen have been investigated as fuels in the HVOF process used to deposit SAM2X5.

While the thickness of a typical coating ranges from 0.4 to 1.0 mm (nominally 15 to 40 mils), adherent coatings with thicknesses of 7.5 mm have been produced. Free-standing plates with thicknesses as great as 20 mm have also been produced. Values of the coating density estimated from weights and dimensions of coated samples ranged from 6.47 to 7.82 g cm^{-3} with an average off ~6.89 g cm^{-3}. These values are compared to the actual density of ~7.65 g cm^{-3} determined for melt-spun ribbons and ingots. Since micrographs indicate that the coatings are almost fully dense

(~7.65 g cm^{-3}), the estimate based upon the weights and dimensions of coated samples (~6.89 g cm^{-3}) is believed to be lower than the actual coating density. Given the number of individual measurements and assumptions involved in a single estimate of coating density, an apparent error of approximately ten to fifteen percent is not surprising. Since the jaws of the micrometer used to measure coating thickness were stopped by the highest points on the rough as-sprayed surface, the measured thickness and volume estimated from the measurement were both biased towards higher than actual values, and the densities calculated with the volume were biased towards lower than actual values.

II.C. Energy Dispersive Spectroscopy

Melt-spun ribbons were prepared by adding 1, 3, 5 and 7 atomic percent molybdenum (Mo) to $Fe_{52.3}Mn_2Cr_{19}Mo_{2.5}W_{1.7}B_{16}C_4Si_{2.5}$ (SAM40), and were designated SAM2X1, SAM2X3, SAM2X5 and SAM2X7, respectively. The SAM2X5 ($Fe_{49.7}Cr_{17.7}Mn_{1.9}Mo_{7.4}W_{1.6}B_{15.2}C_{3.8}Si_{2.4}$) provided adequate corrosion resistance, and was a formulation that could be processed with relative ease. The SAM2X7 composition had a higher calculated pitting-resistance equivalence number (PREN) than the alloys with less molybdenum, and better corrosion resistance than SAM2X5, but was somewhat more difficult to make. The PREN is discussed in detail subsequently.

The target concentrations of heavier elements such as Cr, Mo and W were verified with Energy Dispersive Spectroscopy (EDS). Microanalysis of each sample was performed at three randomly selected locations at 10,000X magnification. Compositional analysis was performed on the smoother side of each melt-spun ribbon (MSR), as the rougher sides were found in some cases to be contaminated with trace amounts of copper, presumably from contact with the copper wheel during the melt spinning process. The concentrations of relatively light elements such as B and C could not be determined with EDS, and were therefore estimated with a simple difference calculation, so that the sum of concentrations for all elements totaled one hundred percent.

II.D. X-Ray Diffraction

The basic theory for X-ray diffraction (XRD) of amorphous materials is well developed and has been published in the literature.[25-26] In the case of amorphous materials, broad peaks are observed. During this study, XRD was done performed with CuK_{α} X-rays, a crystalline graphite analyzer, and a Philips vertical goniometer, using the Bragg-Bretano method. The X-ray optics were self-focusing, and the distance between the X-ray focal point to the sample position was equal to the distance between the sample position and the receiving slit for the reflection mode. Thus, the intensity and resolution were optimized. Parallel vertical slits were added to improve the scattering signal. Step scanning was performed from 20 to 90° (2θ) with a step size of 0.02° at 4 to 10 seconds per point, depending on the amount of sample. The samples were loaded into a low-quartz holder since the expected intensity was very low, thus requiring that the background scattering be minimized.

II.E. Salt Fog Testing

Salt fog tests were conducted according to the standard General Motors (GM) salt fog test, identified as GM9540P, or an abbreviation of that test. The protocol for this test is summarized in Table IV. Reference samples included 1018 carbon steel, Type 316L stainless steel, nickel-based Alloy C-22, Ti Grade 7, and the 50:50 nickel-chromium binary.

II.F. Cyclic Polarization

Cyclic polarization was used to determine the relative susceptibility of candidate amorphous metals to passive film breakdown and localized corrosion. The resistance to localized corrosion is quantified through measurement of the open-circuit corrosion potential (E_{corr}), the breakdown or critical potential ($E_{critical}$), and the repassivation potential (E_{rp}), which can all be determined from such measurements. The greater the difference between the open-circuit corrosion potential and the critical potential (ΔE), the more resistant a material is to modes of localized corrosion such a pitting and crevice corrosion. Spontaneous breakdown of the passive film and localized corrosion require that the open-circuit corrosion potential exceed the critical potential. General corrosion is assumed when E_{corr} is less than $E_{critical}$ ($E_{corr} < E_{critical}$), and localized corrosion is assumed when E_{corr} exceeds $E_{critical}$.[27] Measured values of the repassivation potential (E_{rp}) are sometimes used as conservative estimates of the critical potential ($E_{critical}$).

In the published scientific literature, different bases exist for determining the critical potential from such electrochemical measurements.[28] The breakdown or critical potential has been defined as the potential where the passive current density increases to a level between 1 to 10 μA/cm^2 (10^{-6} to 10^{-5} A/cm^2) while increasing potential in the positive (anodic) direction during cyclic polarization or potential-step testing. The repassivation potential has been defined as the potential where the current density drops to a level indicative of passivity, which has been *assumed* to be between 0.1 to 1.0 μA/cm^2 (10^{-6} to 10^{-7} A/cm^2), while decreasing potential from the maximum level reached during cyclic polarization or potential-step testing. Alternatively, the repassivation potential has been defined as the potential during cyclic polarization where the forward and reverse scans intersect, a point where the measured current density during the reverse scan drops to a level *known* to be indicative of passivity. Details are discussed in the subsequent section.

Cyclic polarization (CP) measurements were based on a procedure similar to ASTM (American Society for Testing and Materials) G-5 and other similar standards with slight modification.[29-32] The ASTM G-5 standard calls for a 1N H_2SO_4 electrolyte, whereas 3.5-molal sodium chloride solution, with and without nitrate additions, natural seawater, and several other synthetic brines were used during this investigation. The natural seawater used in these tests was obtained directly from Half Moon Bay along the northern coast of California. The synthetic brines were based upon concentrated J-13 well water, and are known as simulated dilute water (SDW), simulated concentrated water (SCW), and simulated acidic water (SAW).[27] The exact composition of these brines are summarized in Table V. The ASTM G-5 standard calls for the use of de-aerated solutions, whereas aerated and de-aerated solutions were used here.

Temperature-controlled borosilicate glass (Pyrex) electrochemical cells were used for cyclic polarization and other similar electrochemical measurements. This cell had three electrodes, a working electrode (test specimen), a reference electrode, and a counter electrode. A standard silver silver-chloride electrode, filled with near-saturation potassium chloride solution, was used as the reference, and communicated with the test solution via a Luggin probe placed in close proximity to the working electrode, which minimized Ohmic losses. The electrochemical cell was equipped with a water-cooled junction to maintain the reference electrode at ambient temperature, which thereby maintained integrity of the potential measurement, and a water-cooled condenser, which prevented the loss of volatile species from the electrolyte.

II.G. Linear Polarization

The linear polarization method was used as a method for determining the apparent corrosion rates of the various amorphous metal coatings. The procedure used for linear polarization testing consisted of the following steps: (1) holding the sample for ten seconds at the open circuit potential – OCP; (2) beginning at a potential 20 mV below the OCP, increasing the potential linearly at a constant rate of 0.1667 mV per second to a potential 20 mV above the OCP; (3) recording the current being passed from the counter electrode to the working electrode as a function of potential relative to a standard Ag/AgCl reference electrode; and (4) determining the parameters in the cathodic Tafel line by performing linear regression on the voltage-current data, from 10 mV below the OCP, to 10 mV above the OCP. The slope of this line was the polarization resistance, *Rp* (ohms).[33]

$$R_P = \left(\frac{\partial E}{\partial I}\right)_{E_{corr}} \tag{2}$$

The corrosion current density was then defined in terms of B, R_p and A, the actual exposed area of the sample being tested. The parameter (B) was defined in terms of the slopes of the anodic and cathodic branches of the Tafel line:

$$B = \frac{\beta_a \beta_c}{2.303(\beta_a + \beta_c)} \tag{3}$$

Values of B have been published for a variety of iron-based alloys, and varied slightly from one alloy-environment combination to another.[31] For example, values for carbon steel, as well as Type 304, 304L and 430 stainless steels, in a variety of electrolytes which include seawater, sodium chloride, and sulfuric acid, ranged from 19 to 25 mV. A value for nickel-based Alloy 600 in lithiated water at 288°C was given as approximately 24 mV. Given the value for Alloy 600, a value of 25 mV was also believed to be acceptable for converting the polarization resistance for nickel-based Alloy C-22 to corrosion current. While no values for the Tafel parameter (B) of Fe-based amorphous metals have yet been developed, it was believed that a conservative value of approximately 25 mV was reasonable, based upon the range of published values for several Fe- and Ni-based alloys. The corrosion current in amps (I_{corr}) was then defined as:

$$I_{corr} = \frac{B}{R_p} \tag{4}$$

The corrosion current density, i_{corr} (A cm^{-2}), was defined as the corrosion current, normalized by electrode area, A (cm^2). The corrosion (penetration) rate was calculated from the corrosion current density through application of Faraday's Law.[34]

$$\frac{dp}{dt} = \frac{i_{corr}}{\rho_{alloy} n_{alloy} F} \tag{5}$$

where p was the penetration depth, t was time, i_{corr} was the corrosion current density, ρ_{alloy} was the density of the alloy (g cm^{-3}), n_{alloy} was the number of gram equivalents per gram of alloy, and F was Faraday's constant. The value of n_{alloy} was calculated with the following formula:

$$n_{alloy} = \sum_j \left(\frac{f_j n_j}{a_j} \right) \tag{6}$$

where f_j was the mass fraction of the j^{th} alloying element in the material, n_j was the number of electrons involved in the anodic dissolution process, which was assumed to be congruent, and a_j was the atomic weight of the j^{th} alloying element. Congruent oxidation or dissolution was assumed, which meant that the dissolution rate of a given alloy element was assumed to be proportional to its concentration in the bulk alloy. These equations were used to calculate factors for the conversion of corrosion current density to the corrosion rate. The conversion factors for converting corrosion current density to corrosion rate are approximately: 6.38 to 10.7 $\mu m\ cm^2\ \mu A^{-1}\ yr^{-1}$ for Type 316L stainless steel; 5.57 to 9.89 $\mu m\ cm^2\ \mu A^{-1}\ yr^{-1}$ for Alloy C-22; and 5.39 to 7.89 $\mu m\ cm^2\ \mu A^{-1}\ yr^{-1}$ for SAM2X5, depending upon the exact composition of each alloy within the specified ranges.

The linear polarization method is widely used by the corrosion science community, and was taken directly from standardized ASTM procedures and a NACE Corrosion Engineer's Reference Book.[33] Even so, this method is limited in that it deduces the apparent corrosion rate from a measurement of current density across the entire surface of the sample, and cannot be used to separate general and localized corrosion.

A correction for the junction potential of the reference electrode was performed with the Henderson Equation using ionic properties taken from Bard and Faulkner.[35] Since these corrections were less than approximately 10 mV, it was therefore concluded that no significant error would result from neglecting the correction.

III. EXPERIMENTAL RESULTS

III.A. Amorphous Structure

X-ray diffraction (XRD) was done with SAM2X5 gas-atomized powder identified as Lot # 06-015. Measurements of X-ray intensity as a function of diffraction angle (2θ) are shown in Figure 1. The broad halos observed at 2θ ~ 44° and 78° indicated that the powder was essentially amorphous, with very little residual crystalline structure. This amorphous powder was used to prepare the thermal-spray coatings tested during this study.

XRD data was also obtained with a SAM2X5 thermal spray coating produced with Lot # 06-015 powder, deposited on an Alloy C-22 substrate identified as Sample # CC-22 4019 (Figure 2), and on a Type 316L stainless steel substrate identified as Sample # E316L511 (Figure 3). The broad halo observed at 2θ ~ 44° indicated that the coating was predominately amorphous, and the small sharp peaks are attributed to the presence of minor crystalline phases. These phases are believed to include Cr_2B, WC, $M_{23}C_6$ and bcc ferrite, which are known to have a detrimental effect on corrosion performance. These potentially deleterious precipitates deplete the amorphous matrix of those alloying elements, such as chromium, responsible for enhanced passivity. Coatings with less residual crystalline phase have been observed. The distinctive satellite peak at 2θ ~ 36° may be due to the formation of tungsten carbide (WC) during the thermal spray process. Note that this satellite is absent in the XRD data for the feed powder. The structure seen near 2θ ~ 60° may be due to bcc ferrite, and has been correlated with increased susceptibility of such amorphous metal coatings to corrosion. Other structure is due to $M_{23}C_6$ and Cr_2B.

III.B. Salt-Fog Performance

Early salt fog tests confirmed the corrosion resistance of the corrosion resistance of thermal spray coatings of SAM2X5 relative to other alloys with less molybdenum. As previously discussed, these coatings were deposited with the high-velocity oxy-fuel (HVOF) process, using amorphous metal powders. HVOF coatings of Type 316L stainless steel and the parent alloy, SAM40, showed significant corrosion after only 13 cycles in the GM salt fog test. In contrast, HVOF coatings on nickel-based Alloy C-22 and amorphous SAM2X5 showed no obvious corrosion after more than 60 cycles.

Several samples were tested with the GM salt fog test, and are shown after eight (8) full cycles in Figure 4. These samples include: (Samples # A14) a reference sample of 1018 steel; Sample # 316-170, an early HVOF coating of 316 stainless steel on Type 316L stainless steel substrate; Sample # 316-238, an early HVOF coating of Alloy C-22 on Type 316L stainless steel substrate; Sample # 316-041, an early HVOF SAM40 coating on Type 316L stainless steel substrate; Sample # 316-095, an early HVOF coating of SAM40X3 on Type 316L stainless steel substrate; Sample # 316L-W9, a recent HVOF coating of SAM2X5 on Type 316L stainless steel substrate; and Sample # C22-W21, a recent HVOF coating of SAM2X5 on nickel-based Alloy C-22 substrate. Arrows added to the image of Sample # 316-095 pinpoint very small spots that are suspected loose iron oxide. There were no suspected iron oxide spots observed on Sample # 316L-W9.

The coated cylinder shown in Figure 5 is a half-scale model of a container for the storage of spent nuclear fuel, and was fabricated from Schedule-10s Type 316L stainless-steel pipe. A hydrogen-fueled air-breathing HVOF thermal-spray process, based upon the JK-2000 gun, was used to coat the outer diameter with SAM2X5, using Lot # 06-015 powder. This coated container was then subjected to eight (8) full cycles in the GM salt fog test. No loose iron oxide was observed with this thermally sprayed amorphous metal coating, while substantial attack of the 1018 carbon steel was observed. A single spot showed iron oxide, which is an area where the coating appears to have been accidentally removed by gouging during handling. Slight discoloration was observed in a band of coating near the center of the container, and on a spot on the bottom edge of the container. Such amorphous metal coatings may therefore provide a good means for protecting less corrosion resistant surfaces.

III.C. Electrochemical Behavior – Cyclic Polarization Measurements

Studies have been conducted previously to assess the sensitivity of these iron-based amorphous metals to devitrification, which can occur at elevated temperature. Melt-spun ribbons of Fe-based amorphous metals were intentionally devitrified by heat treating them at various temperatures for one hour. After heat treatment, the samples were evaluated in high temperature seawater (90°C) with cyclic polarization, to determine the impact of the heat treatment on passive film stability and corrosion resistance. The temperatures used for the heat treatment were: 150, 300, 800 and 1000°C. In general, corrosion resistance was maintained below the crystallization temperature, and lost after prolonged aging at higher temperatures.

Figure 6 shows CP data for a melt-spun ribbon (MSR) and for a HVOF coating of SAM2X5 in 3.5-molal solution of NaCl at 90°C. The SAM2X5 coating was prepared by depositing Lot # 06-

015 powder on a Type 316L stainless steel substrate, using a hydrogen-fueled thermal spray process. CP data are also shown for two austenitic neutron-absorbing steels, the first being a Ni-Cr-Mo-Gd alloy and the second being a borated stainless steel. All potentials were measured relative to the standard Ag/AgCl reference electrode.

By a very large margin, the greatest passive film stability was observed with the SAM2X5 melt-spun ribbon. A very low passive current density ($\leq 1\ \mu A\ cm^{-2}$) was maintained during the anodic potential scan, from the OCP of approximately –0.2 V, to the passive film breakdown potential of ~ 0.9 V. After scan reversal at a relatively high potential of ~ 1.1 V, a relatively small hyseresis loop was observed, with a repassivation potential found between 0.8 and 0.7 V.

In the case of the borated stainless steel, passivity was maintained during the anodic potential scan, from the OCP of approximately –0.6 V to a value of approximately –0.3 V, where passive film breakdown occurred. Following potential reversal at approximately –0.2 V, a large hysteresis loop was observed, with no subsequent repassivation observed, which indicates that this alloy could experience spontaneous passive film breakdown in this type of environment.

In the case of the Ni-Cr-Mo-Gd alloy, a broad oxidation peak was observed during the anodic potential scan from the OCP, which was between –0.5 and –0.6 V, and the reversal potential, which was approximately 0.2 V. This oxidation peak may have resulted in the formation of a relatively conductive surface oxide. Following voltage reversal, a small hysteresis loop was observed, with intersection of the forward and reverse scans at 0 V, which may be the repassivation potential.

In the case of the SAM2X5 coating, which was also prepared with Lot # 06-015 powder and a hydrogen-fueled HVOF process, the current density increased steadily during the anodic potential scan from approximately 10 $\mu A\ cm^{-2}$ at the OCP of approximately –0.4 V to almost 5,000 $\mu A\ cm^{-2}$ at the reversal potential, which was between 0.9 and 1.0 V. This steady rise in current density indicated that this coating had relatively poor passive film stability in concentrated chloride solutions near their boiling point. The forward and reverse scans intersected at approximately –0.3 V, which may have defined the repassivation potential.

Figure 7 shows CP data for HVOF coatings of SAM2X5 in 3.5-molal NaCl solution at 30 and 90°C, and for HVOF coating of SAM2X5 in 3.5-molal NaCl solution at 90°C after the addition of 0.525-molal KNO_3. The inhibitory effect of nitrate was found to be very large, which was expected in such concentrated chloride electrolytes.

III.D. Electrochemical Behavior – Corrosion Potential & Linear Polarization

Samples were produced by depositing SAM2X5 powder (Lot #06-015) on Alloy C-22 substrates with an air-breathing hydrogen-fueled HVOF process. In the case of the linear-polarization corrosion rate (LPCR) and OCP measurements, the Alloy C-22 substrates were cylindrical rods, each having one hemispherical tip. The length and diameter of each rod were 20.32 cm (nominally 8 inches) and 1.588 cm (nominally 5/8 inches), respectively. The SAM2X5 coating was deposited on the outer diameter of the barrel, as well as on the hemispherical tips, with a thickness of approximately 433 ± 51 microns (nominally 17±2 mils).

As shown in Figure 8, linear polarization was used to monitor the apparent corrosion rates of the SAM2X5-coated rods in seven relevant environments for 133 days. These environments were: (1) natural seawater at 90°C; (2) 3.5-molal NaCl solution at 30°C; (3) 3.5-molal NaCl solution at 90°C; (4) 3.5-molal NaCl solution with 0.525-molal KNO_3 at 90°C; (5) simulated dilute water, referred to as SDW, at 90°C; (6) simulated concentrated water, referred to as SCW, at 90°C; and (7) simulated acidic water, referred to as SAW, at 90°C. The corresponding final values of the apparent corrosion rates were: (1) 12.3 μm/yr; (2) 2.91 μm/yr; (3) 176 μm/yr; (4) 2.83 μm/yr; (5) 2.61 μm/yr; (6) 12.4 μm/yr; and (7) 81.1 μm/yr, respectively. Clearly, the greatest electrochemical activities, which were quantified in terms of the measured LPCR values, were observed in 3.5-molal NaCl solution and SAW, both at 90°C, with the SAW having an acidic pH. The next highest LPCR values were observed in natural seawater and SCW, both at 90°C with near-neutral pH. Not surprisingly, the lowest LPCR values were observed in 3.5-molal NaCl solution and SDW, both at 30°C with near-neutral pH, as well as in 3.5-molal NaCl solution with 0.525-molal KNO_3 at 90°C. The nitrate inhibitor reduced the LPCR value observed in 3.5-molal NaCl solution from 176 to 2.83 μm/yr, nearly two orders-of-magnitude. The bar chart shown in the following figure summarizes these trends in corrosion rate graphically. The corresponding values of the OCP are shown in Figure 9.

Figure 10 shows the SAM2X5-coated rods of Alloy C-22 used for linear polarization and OCP measurements after 135 days immersion in the seven environments. Note that the samples were removed for weight and dimensional measurement two days after linear polarization measurements were finished. In natural seawater at 90°C there was relatively little corrosive attack of much of the coated surface, although discrete nodules of corrosion product formed at several sites on the exposed coated cylinder. Dark corrosion products were formed at the edge of the insulating sheath, which may have formed a slight crevice (corresponding photograph, left end of rod). The epoxy used to mask the hemispherical tip of the rod, and to seal the insulating sheath turned black in color during the test.

The effects of temperature and nitrate inhibitor on the corrosion of SAM2X5 are evident from the samples tested in 3.5-molal NaCl solution shown in Figure 10. In 3.5-molal NaCl solution at 30°C, most of the coating experienced light corrosion, though discrete nodules of corrosion product formed at several sites on the barrel, close to the hemispherical tip. Here too dark corrosion products formed at the edge of the insulating sheath (corresponding photograph, left end of rod). The epoxy used to mask the hemispherical tip of the rod, and to seal the insulating sheath turned black in color during the test. In 3.5-molal NaCl solution at 90°C, substantial localized corrosion of the coating occurred, with numerous nodules of corrosion product formed over much of the surface. There may have been some corrosion underneath the insulating sheath (corresponding photograph, left end of rod). In 3.5-molal NaCl solution with 0.525-molal KNO_3 at 90°C, there was some discoloration due to slight corrosion. The benefits of nitrate inhibitor in such near-boiling concentrated chloride solutions are easily seen by comparing the photographs for SAM2X5 in 3.5-molal NaCl solution at 90°C, with and without nitrate.

Corrosion in the synthetic brines based upon concentrations of well J-13 water is shown in Figure 10. In SDW at 90°C, there was no visible evidence of corrosion, and the sample was in pristine condition after exposure. In SCW at 90°C, there was some discoloration, but relatively little corrosion on the barrel of the coated cylinder. The white deposit covering the metallic coating was identified as precipitated salt from the test solution. The insulating sheath covering the coated cylinder may have formed a crevice, with dark corrosion products formed at its mouth (corresponding photograph, left end of rod). The epoxy used to mask the hemispherical tip of the rod, and to seal the insulating sheath turned black in color during the test. In SAW at 90°C, despite the relatively high electrochemical activity, there was no obvious evidence of corrosion, and the sample appeared to be in pristine condition after exposure. The epoxy used to mask the hemispherical tip of the rod, and to seal the insulating sheath turned black in color during the test.

III.E. Corrosion Rates – Based on Weight-Loss & Dimensional Measurements

Weight-loss and dimensional measurements were used to determine the corrosion rates of SAM2X5 coatings (Lot # 06-015 powder) on Alloy C-22 weight-loss samples, as shown in Figure 11. Depending upon the assumed coating density, these rates were determined to be: (1) 14.3-15.9 μm/yr in natural seawater at 90°C; (2) 8.4-9.3 μm/yr in 3.5-molal NaCl solution at 30°C; (3) 26.1-29.7 μm/yr in 3.5-molal NaCl solution at 90°C; (4) 4.6-5.1 μm/yr in 3.5-molal NaCl and 0.525-molal KNO_3 solution at 90°C; (5) 8.3-9.4 μm/yr in SDW at 90°C; (6) 2.8-3.0 μm/yr in SCW at 90°C; and (7) 16.5-18.1 μm/yr in SAW at 90°C. In the case of 3.5-molal NaCl solution at 90°C, the electrochemical measurement over predicted the actual corrosion rate determined with weight loss and dimensional measurements by a factor of about six. In the case of SAW at 90°C, the electrochemical measurement also over predicted the actual corrosion rate determined by weight loss and dimensional measurements, this time by a factor of about five. While electrochemical measurements such as linear polarization could be used to determine qualitative trends in corrosion rates during these long-term immersion tests, absolute values in the most aggressive electrolytes were over predicted by a factor of five-to-six. In contrast, the corrosion rates determined with linear polarization proved to be non-conservative in the more benign electrolytes, and under predicted the actual corrosion rates by a factor of about two-to-three (×2 to ×3). Linear polarization is a valuable method for determining qualitative trends in corrosion rate in real time, but cannot measure corrosion rates accurately enough for reliable long-term prediction.

Weight-loss and dimensional measurements were also used to determine the corrosion rates of SAM2X5 coatings (Lot # 06-015 powder) on Alloy C-22 crevice-corrosion samples after 135 days immersion, as shown in Figure 12. Depending upon the assumed coating density, these rates were determined to be: (1) 14.7-17.3 μm/yr in natural seawater at 90°C; (2) 8.8-9.9 μm/yr in 3.5-molal NaCl solution at 30°C; (3) 28.8-32.5 μm/yr in 3.5-molal NaCl solution at 90°C; (4) 4.2-4.3 μm/yr in 3.5-molal NaCl solution with 0.525-molal KNO_3 at 90°C; (5) 8.2-9.5 μm/yr in SDW at 90°C; (6) 2.7-3.2 μm/yr in SCW at 90°C; and (7) 19.7-22.5 μm/yr in SAW at 90°C.

Figure 13 shows SAM2X5-coated weight-loss and crevice samples, fabricated from Alloy C-22 plates, after 135 days immersion in the seven environments. In natural seawater at 90°C, SAM2X5-coated samples identified as C22-W1, C22-W2, C22-C1 and C22-C2 showed reddish-brown corrosion products on the surface due to corrosion. There was a scalloped crevice corrosion pattern on both the SAM2X5-coated front side of the crevice samples, as well as on the Alloy C-22 back side of the crevice samples. There was also some corrosion on the edge of the samples, at the coating-substrate interface.

The effects of temperature and nitrate inhibitor on the corrosion of SAM2X5 were evident from the weight-loss and crevice samples tested in 3.5-molal NaCl solution, shown in Figure 13. In 3.5-molal NaCl solution at 30°C, SAM2X5-coated samples identified as C22-W3, C22-W4, C22-C3 and C22-C4 had reddish-brown stain on the surface, with some sparse pitting corrosion. In 3.5-molal NaCl solution at 90°C; SAM2X5-coated samples identified as C22-W5, C22-W6, C22-C5 and C22-C6 had heavier reddish-brown stains, and heavier pitting corrosion than the samples exposed at lower temperature. In 3.5-molal NaCl solution with 0.525-molal KNO_3 at 90°C, SAM2X5-coated samples identified as C22-W7, C22-W8, C22-C7 and C22-C8 showed slight reddish-brown stains on the surface, while the crevice-corrosion samples showed sparse pitting corrosion around the perimeter of the samples.

Corrosion of SAM2X5 weight-loss and crevice samples in the synthetic brines based upon concentrations of well J-13 water are also shown in Figure 13. In SDW at 90°C, SAM2X5-coated samples identified as C22-W9, C22-W10, C22-C9 and C22-C10 showed slight discoloration, but no evidence of corrosion. In SCW at 90°C, SAM2X5-coated samples identified as C22-W11, C22-W12, C22-C11 and C22-C12 showed slight discoloration, but no significant corrosion. In SAW at 90°C, samples, identified as C22-W13, C22-W14, C22-C13 and C22-C14 showed slight discoloration, perhaps due to residue adhering to the rough porous surface, but no significant corrosion. An area stained with corrosion product was observed neat the bolt hole in crevice sample C22-13. An array of cracks was observed in the center of the weight-loss samples identified as C22-W13 and C22-14, with corrosion products inside the crack. The stress responsible for driving this cracking process appears to be due to aluminum oxide (Al_2O_3) grit-blasting particles at the coating-substrate interface, as will be discussed in the subsequent section. Since this type of cracking was only observed in electrolytes with acidic pH, it is possible that this cracking may be due in part to the coating's absorption of hydrogen by the coating near the cracks. The galvanic coupling of the anodic oxidation of metal within the crack could drive electrochemical hydrogen reduction near the cracks.

III.F. Characterization of Corrosive Attack of Samples

Backscattered electron (BSE) images of a SAM2X5 sample prepared with completely amorphous powder (Lot # 06-015) after 135 days in natural seawater at 90°C are shown in Figure 14. The image on the left shows a cross-section of a superficial spot of iron oxide, and the image on the right shows an area without corrosion. The image on the right represents a larger area fraction of the surface. These images show that the coatings have no interconnected porosity, and are virtually full density. Energy dispersive spectroscopy (EDS) maps for iron and oxygen corresponding to the BSE images shown in Figure 14 are shown in Figure 15. The iron and oxygen maps on the left show a superficial spot of iron oxide, in cross-section, and the maps on the right show an area of coating without any corrosion. There is no cracking in the coating, and not penetration of corrosion product beneath the surface. The images on the right are more representative of the surface, and show no superficial iron oxide. The BSE cross-sectional images for samples tested other environments where iron-oxides spots formed on the surface, such as 3.5 molal NaCl solutions at 90°C, are similar in appearance.

It is important to point out that in similar experiments with coatings produced much earlier, and prepared with partially de-vitrified SAM2X5 powder (Lot #05-079), more plentiful iron oxide spots observed on the surface, and in some cases, cracks penetrated through the entire coating thickness to the substrate at these corrosion sites. It is believed that these cracks formed around the perimeter of a relatively large, partially de-vitrified particle that was embedded in the coating. High-quality spherical amorphous-metal powders that can be pneumatically conveyed with ease in the HVOF process are essential. Re-melting of SAM2X5 powder during gas atomization is not recommended at the present time, since undesirable crystalline phases have been observed during such recycling. The quality of the powder should be verified with both SEM and XRD prior to use. . These specific problems appear to have been resolved with the current generation of optimized amorphous-metal powders and coatings reported here (TNC Lot #06-015 Powder, Plasma Tech HVOF Process).

Backscattered electron (BSE) and secondary electron (SE) images of a SAM2X5 coating sample prepared with completely amorphous powder (Lot # 06-015) after 135 days in SAW at 90°C are shown in Figure 16. The cross-sectional BSE image on the left shows a cracked and corroded region in center of sample. The SE image on the right shows the same region. The presence of an aluminum oxide (Al_2O_3) particle is shown at the base of the crack. The composition of this particle was verified as aluminum oxide, or alumina, with the EDS maps shown in Figure 17. The two maps on the left confirm the iron content of the coating, and the nickel content of the Alloy C-22 substrate. The two maps on the right show that the particle at the coating-substrate interface consists primarily of aluminum and oxygen. While the reduction of hydrogen ions in this relatively acidic environment sets the stage for potential hydrogen absorption, and may therefore promote crack initiation and propagation, the stress responsible for driving this crack appears to have been induced by an Al_2O_3 particle at the interface between the coating and the substrate. This particle is believed to have been embedded at the interface during the alumina grit blasting of the sample prior to HVOF coating. Proper grit blasting is essential to achieve high bond strengths. The elimination of residual grit blasting media, used in surface preparation, is critical. This can be better accomplished through the use of ultrasonic cleaning.

IV. CONCLUSIONS

An iron-based amorphous metal, $Fe_{49.7}Cr_{17.7}Mn_{1.9}Mo_{7.4}W_{1.6}B_{15.2}C_{3.8}Si_{2.4}$ (SAM2X5), with very good corrosion resistance was developed. This material was produced as a melt-spun ribbon, as well as gas atomized powder and a thermal-spray coating. Chromium, molybdenum and tungsten provided corrosion resistance, and boron enabled glass formation. The high boron content of this particular amorphous metal made it an effective neutron absorber, and suitable for criticality control applications. Earlier studies have shown that ingots and melt-spun ribbons of these materials have good passive film stability in these environments. Thermal spray coatings of these materials have now been produced, and have undergone a variety of corrosion testing, including both atomospheric and long-term immersion testing. The modes and rates of corrosion have been determined in the various environments, and are reported here.

The high boron content of $Fe_{49.7}Cr_{17.7}Mn_{1.9}Mo_{7.4}W_{1.6}B_{15.2}C_{3.8}Si_{2.4}$ (SAM2X5) makes it an effective neutron absorber, and suitable for criticality control applications. Average measured values of the neutron absorption cross section in transmission (Σ_t) for Type 316L stainless steel, Alloy C-22, borated stainless steel, a Ni-Cr-Mo-Gd alloy, and SAM2X5 have been determined to be approximately 1.1, 1.3, 2.3, 3.8 and 7.1 cm^{-1}, respectively, and are discussed in detail in a separate publication.[17] This material and its parent alloy have been shown to maintain corrosion resistance up to the glass transition temperature, and to remain in the amorphous state after receiving relatively high neutron dose.

In general, melt-spun ribbons of SAM2X5, and other similar iron-based amorphous metals, have better passive film stability and corrosion resistance than thermal-spray coatings, in a broad range of aggressive environments. However, the coating process for these amorphous alloys has not progressed to the point where thermal-spray coatings can be produced with corrosion resistance comparable to or better than other neutron absorbing steels, including but not limited to borated stainless steel.

Type 316L stainless-steel cylinders were coated with SAM2X5, and served as half-scale models of containers for the storage of spent nuclear fuel. SAM2X5-coated cylinders and plates were subjected to eight full cycles in the GM salt fog test. No loose iron oxide was observed with this thermally sprayed amorphous metal coating, while substantial attack of the 1018 carbon steel was observed. A single spot showed iron oxide, which is an area where the coating appears to have been accidentally removed by gouging during handling. Slight discoloration was observed in a band of coating near the center of the container, and on a spot on the bottom edge of the container. Such amorphous metal coatings may therefore provide a good means for protecting less corrosion resistant surfaces.

Corrosive attack of the SAM2X5 coatings after immersion in the seven aggressive test solutions for 135 days is characterized as follows:

1. Natural Seawater at 90°C – moderate superficial corrosion
2. Concentrated Chloride (3.5 m NaCl) at 30°C – moderate superficial corrosion
3. Concentrated Chloride (3.5 m NaCl) at 90°C – relatively heavy superficial corrosion
4. Concentrated Chloride (3.5 m NaCl + 0.525 m KNO_3) at 90°C – light superficial corrosion
5. SDW at 90°C – non-existent to light superficial corrosion
6. SCW at 90°C – non-existent to light superficial corrosion
7. SAW at 90°C – non-existent to light corrosion – possible hydrogen-assisted cracking

In the low-pH SAW environment, an array of fine cracks was observed in the center of all weight-loss samples, with corrosion products inside the crack. The stress responsible for driving this cracking process appears to be due to aluminum oxide (Al_2O_3) grit-blasting particles at the coating-substrate interface. Since this type of cracking was only observed in electrolytes with acidic pH, it is possible that this cracking may be due in part to the coating's absorption of hydrogen by the coating near the cracks. The galvanic coupling of the anodic oxidation of metal within the crack could drive electrochemical hydrogen reduction near the cracks.

Trends in corrosion rates measured with linear polarization (LPCR values) were consistent with trends in corrosion rates based upon weight-loss and dimensional change. In seawater at 90°C, the LPCR values were accurate predictors of corrosion rates based upon weight-loss and dimensional change. However, the highest LPCR values, which were measured in 3.5-molal NaCl solution, SCW and SAW at 90°C, were found to be overly conservative. The lowest LPCR values, which were measured in 3.5-molal NaCl solution at 30°C, 3.5-molal NaCl solution with 0.525-molal KNO_3 (nitrate inhibitor) at 90°C, and SDW at 90°C, and proved to be insufficiently conservative.

SAM2X5-coated cylinders used for LPCR and OCP determination in SDW and SAW 90°C showed no discoloration or iron oxide spots on the outer diameter (barrel), and no corrosion products at the interface between the coating and the insulating sheath. An identical cylinder used for LPCR and OCP determination in SCW 90°C showed no discoloration or iron oxide spots on the outer diameter (barrel), but the formation of patches of iron oxide at the interface between the coating and the insulating sheath, and a white film of salt precipitates from the rapid drying of the electrolyte during removal of the sample from the test solution.

ACKNOWLEDGMENTS

This work was performed by Lawrence Livermore National Laboratory under Contract Number W-7405-Eng-48 and under the auspices of the United States Department of Energy. Work was co-sponsored by the Office of Civilian and Radioactive Waste Management (OCRWM) of the United States Department of Energy (DOE), and the Defense Science Office (DSO) of the Defense Advanced Research Projects Agency (DARPA). The guidance of Jeffrey Walker at DOE OCRWM and Leo Christodoulou at DARPA DSO is gratefully acknowledged.

Recent salt-fog testing has been conducted by E-Labs in Fredericksburg, Virginia by Ken Maloy and co-workers. Several substantive scientific comments were provided by Thomas Wolery at LLNL, and served to improve this work.

REFERENCES

1. M. Telford: The case for bulk metallic glass. *Materials Today*, **3,** 36-43 (2004).
2. N. R. Sorensen and R. B. Diegle: Corrosion of amorphous metals. In *Corrosion, Metals Handbook*, 9th Ed., Vol. 13, edited by J. R. Davis and J. D. Destefani (ASM Intl., Metals Park, OH, 1987), pp. 864-870.
3. D. E. Polk and B. C. Giessen: Overview of principles and applications. Chapter 1, in *Metallic Glasses*, edited by J. J. Gilman and H. J. Leamy (ASM Intl., Metals Park, OH, 1978), pp. 2-35.
4. K. Kishitake, H. Era, and F. Otsubo: Characterization of plasma sprayed Fe-10Cr-10Mo-(C,B) amorphous coatings. *J. Thermal Spray Technology*, **5** (2), 145-153 (1996).
5. S. Pang, T. Zhang, K. Asami, and A. Inoue: Effects of chromium on the glass formation and corrosion behavior of bulk glassy Fe-Cr-Mo-C-B alloys. *Materials Transactions*, **43** (8), 2137-2142 (2002).
6. S. J. Pang, T. Zhang, K. Asami, and A. Inoue: Synthesis of Fe-Cr-Mo-C-B-P bulk metallic glasses with high corrosion resistance. *Acta Materialia*, **50**, 489-497 (2002).
7. F. Guo, S. J. Poon, and G. J. Shiflet: Metallic glass ingots based on yttrium. *Metallic Applied Physics Letters*, **83** (13), 2575-2577 (2003).
8. Z. P. Lu, C. T. Liu, and W. D. Porter: Role of yttrium in glass formation of Fe-based bulk metallic glasses. *Metallic Applied Physics Letters*, **83** (13), 2581-2583 (2003).
9. V. Ponnambalam, S. J. Poon, and G. Shiflet: Fe-Mn-Cr-Mo-(Y,Ln)-C-B (Ln=Lanthanides) bulk metallic glasses as formable amorphous steel alloys. *J. Materials Research*, **19** (5), 1320, 2004.
10. J. C. Farmer, J. J. Haslam, S. D. Day, D. J. Branagan, C. A. Blue, J. D. K. Rivard, L. F. Aprigliano, N. Yang, J. H. Perepezko, and M. B. Beardsley: Paper PVP2005-71664, Pressure Vessels and Piping Division Conference, Denver, CO, July 17-21, 2005 (ASME, Three Park Avenue, New York, NY, 2005).
11. J. C. Farmer, J. J. Haslam, S. D. Day, T. Lian, R. Rebak, N. Yang, and L. Aprigliano: Corrosion resistance of iron-based amorphous metal coatings. Paper PVP2006-ICPVT11-93835, *Pressure Vessels and Piping Division Conference*, Vancouver, BC, July 23-27, 2006 (ASME, Three Park Avenue, New York, NY, 2006).
12. D. Chidambaram, C. R. Clayton, and M. R. Dorfman: Evaluation of the electrochemical behavior of HVOF-sprayed alloy coatings. *Surface and Coatings Technology*, **176**, 307-317 (2004).
13. D. J. Branagan, Method of modifying iron-based glasses to increase crystallization temperature without changing melting temperature. U.S. Patent Application No. 20040250929, Filed December 16, 2004 (Published by U.S. Patent and Trademark Office).
14. D. J. Branagan: Properties of amorphous/partially crystalline coatings. U.S. Patent Application No. 20040253381, Filed December 16, 2004 (Published by U.S. Patent and Trademark Office).
15. H. P. Hack: Crevice corrosion behavior of molybdenum-containing stainless steel in seawater. *Materials Performance*, **22** (6) 24–30 (1983).

16. A. I. Asphahani: Corrosion resistance of high performance alloys. *Materials Performance*, **19** (12) 33–43 (1980).
17. R. B. Rebak and P. Crook: Improved pitting and crevice corrosion resistance of nickel and cobalt based alloys. In *Proc. Symposium on Critical Factors in Localized Corrosion III*, 194th Meeting of the Electrochemical Society, Boston, Massachusetts, November 1-6, 1998, Vol. 98-17 (ECS, Pennington, NJ, 1999), pp. 289-302.
18. Z. Szklarska-Smialowska: Pitting resistance equivalence number, effect of alloying elements on stainless steels and Ni-base alloys. Chapter 13, in *Pitting and Crevice Corrosion* (NACE Intl., Houston, TX, 2005), p. 318-321.
19. 4. A. J. Sedriks: Introduction, pitting. Chapter 4, in *Corrosion of Stainless Steels* (J. Wiley & Sons, Inc., New York, NY, 1996), p. 111-113.
20. D. C. Agarwal and M. Kohler: Alloy 33, a new material resisting marine environment. Paper 424, *Corrosion 97* (NACE Intl., Houston, TX 1997).
21. C. Thornton and C. Cooper: Overmatching superalloy consumable Inco-weld, 686CPT broadens its applications to include welding super austenitic and super duplex stainless steels. In *Stainless Steel World* (KCI Publishing BV 1, 2004).
22. J. Farmer, J. Haslam, S. Day, T. Lian, C. Saw, P. Hailey, J-S. Choi, R. Rebak, N. Yang, R. Bayles, L. Aprigliano, J. Payer, J. Perepezko, K. Hildal, E. Lavernia, L. Ajdelsztajn, D. J. Branagan, and M. B. Beardsely: A high-performance corrosion-resistant iron-based amorphous metal – the effects of composition, structure and environment on corrosion resistance. Proc. Scientific Basis for Nuclear Waste Management XXX, Materials Research Society Symposium Series, Vol. 985 (MRS, Warrendale, PA, 2006).
23. T. Lian, D. Day, P. Hailey, J-S. Choi, and J. Farmer: Comparative study on the corrosion resistance of Fe-based amorphous metal, borated stainless steel and Ni-Cr-Mo-Gd alloy. Proc. Scientific Basis for Nuclear Waste Management XXX, Materials Research Society Symposium Series, Vol. 985 (MRS, Warrendale, PA, 2006).
24. J-S. Choi, C. Lee, J. Farmer, D. Day, M. Wall, C. Saw, M. Boussoufi, B. Liu, H. Egbert, D. Branagan, and A. D'Amato: Application of neutron-absorbing structural amorphous metal coatings for spent nuclear fuel container to enhance criticality safety controls. Proc. Scientific Basis for Nuclear Waste Management XXX, Materials Research Society Symposium Series, Vol. 985 (MRS, Warrendale, PA, 2006).
25. C. K. Saw: In *X-ray Scattering Techniques for Characterization Tools in the Life Sciences, Nanotechnologies for the Life Science*, edited by Challa Kumar (Wiley-VCH Verlag GmbH and Company, KGaA, Weinheim, 2006).
26. C. K. Saw and R. B. Schwarz: Chemical short-range order in dense random-packed models. *J. Less-Common Metals*, **140**, 385-393 (1988).
27. J. Farmer, S. Lu, D. McCright, G. Gdowski, F. Wang, T. Summers, P. Bedrossian, J. Horn, T. Lian, J. Estill, A. Lingenfelter, and W. Halsey: General and localized corrosion of high-level waste container in Yucca Mountain. Pressure Vessel and Piping Conference, Seattle, WA, July 23-27, 2000, In *Transportation, Storage, and Disposal of Radioactive Materials*, PVP Vol. 408 (ASME, Three Park Avenue, New York, NY, 2000), pp. 53-70.
28. K. A. Gruss, G. A. Cragnolino, D. S. Dunn, and N. Sridar: Repassivation potential for localized corrosion of alloys 625 and C22 in simulated repository environments. Paper 149, *Corrosion 98* (NACE Intl., Houston, TX, 1998).

29. Standard reference test method for making potentiostatic and potentiodynamic anodic polarization measurements. Designation G 5-94, In *1997 Annual Book of American Society for Testing and Materials Standards,* Section 3, Vol. 3.02 (ASTM, 1997), pp. 54–57.
30. Standard reference test method for making potentiostatic and potentiodynamic anodic polarization measurements. Designation G 5-87, In *1989 Annual Book of American Society for Testing and Materials Standards*, Section 3, Vol. 3.02 (ASTM, 1989), pp. 79–85.
31. Standard practice for conventions applicable to electrochemical measurements in corrosion testing. Designation G 3-89, In *1997 Annual Book of American Society for Testing and Materials Standards*, Section 3, Vol. 3.02, (ASTM, 1997), pp. 36–44.
32. Standard test method for conducting cyclic potentiodynamic polarization measurements for localized corrosion susceptibility of iron-, nickel-, or cobalt-based alloys. Designation G 61-86, In 1997 Annual Book of American Society for Testing and Materials Standards, Section 3, Vol. 3.02 (ASTM, 1997), pp. 231–235.
33. R. S. Treseder, R. Baboian, and C. G. Munger: Polarization resistance method for determining corrosion rates. In *Corrosion Engineer's Reference Book*, 2nd Ed. (NACE Intl., Houston, TX, 1991), pp. 65-66.
34. D. A. Jones: Electrochemical kinetics of corrosion – Faraday's law. Chapter 3, in *Principles and Prevention of Corrosion*, 2nd Ed., Section 3.1.1, Equations 3-5 (Prentice Hall, Upper Saddle River, NJ, 1996), pp. 75–76.
35. A. J. Bard and L. R. Faulkner: Potentials and thermodynamics of cells – liquid junction potentials. Chapter 2, in *Electrochemical Methods, Fundamentals and Applications*, Section 2.3, Table 2.3.2, Equation 2.3.39 (John Wiley and Sons, New York, NY, 1980), p. 67, 71.

TABLES

Table I – Target compositions in atomic percent used to prepare samples.

Alloy	Specification / Formula	Fe	Cr	Mn	Mo	W	B*	C*	Si	Ni	Co	Total
Type 316L	UNS S31603	68.0	18.0	1.5	1.5				1.0	10.0		100
Alloy C-22	UNS N06022	4.0	25.0	0.1	8.0	1.4			1.0	60.0	0.5	100
SAM40	$Fe_{52.3}Mn_2Cr_{19}Mo_{2.5}W_{1.7}B_{16}C_4Si_{2.5}$	52.3	19.0	2.0	2.5	1.7	16.0	4.0	2.5			100
SAM2X1	$(SAM40)_{99} + Mo_1$	51.8	18.8	2.0	3.5	1.7	15.8	4.0	2.5			100
SAM2X3	$(SAM40)_{97} + Mo_3$	50.7	18.4	1.9	5.4	1.6	15.5	3.9	2.4			100
SAM2X5	$(SAM40)_{95} + Mo_5$	49.7	18.1	1.9	7.4	1.6	15.2	3.8	2.4			100
SAM2X7	$(SAM40)_{93} + Mo_7$	48.6	17.7	1.9	9.3	1.6	14.9	3.7	2.3			100

Table II – Thermal analysis data (DTA or DSC) for Fe-based glass forming alloys, including SAM2X5 ($Fe_{49.7}Cr_{17.7}Mn_{1.9}Mo_{7.4}W_{1.6}B_{15.2}C_{3.8}Si_{2.4}$), suitable for thermal spray deposition.

Alloy	T_g (°C)	T_x (°C)	T_m (°C)	T_L (°C)	T_{rg}
SAM40	568-574	623	1110	1338	0.52
SAM2X1	575	620	1124	1190-1210	0.51
SAM2X3	578	626	1131	1190-1210	0.51
SAM2X5	579	628	1133	1190-1210	0.51
SAM2X7	573	630	1137	1190-1210	0.50

Table III – Neutron absorption cross-sections for HVOF coating of Alloy C-22.

Plate ID	Transmission Cross Section Σ_t (cm^{-1})
Type 316L Stainless Steel	**1.07**
Nickel-Based Alloy C-22	**1.29**
Borated Stainless Steel (182193)	1.67
Borated Stainless Steel (182194)	2.21
Borated Stainless Steel (182196)	2.6
Borated Stainless Steel (03180)	2.65
Borated Stainless Steel Average	**2.28**
Borated Stainless Steel Standard Deviation	**0.45**
Ni-Cr-Mo-Gd (NiGd)	3.77
Ni-Cr-Mo-Gd (NiGd)	3.79
Ni-Cr-Mo-Gd (NiGd)	3.91
Ni-Cr-Mo-Gd (NiGd)	3.89
Ni-Cr-Mo-Gd (NiGd) Average	**3.84**
Ni-Cr-Mo-Gd (NiGd) Standard Deviation	**0.07**
HVOF SAM2X5 with Powder Lot # 05-079 (M18W3)	6.52
HVOF SAM2X5 with Powder Lot # 05-079 (M10S14)	7.65
HVOF SAM2X5 with Powder Lot # 06-015 (316LC1)	5.82
HVOF SAM2X5 with Powder Lot # 06-015 (316LC2)	6.73
HVOF SAM2X5 with Powder Lot # 06-015 (316LW1)	7.18
HVOF SAM2X5 with Powder Lot # 06-015 (316LW2)	7.01
HVOF SAM2X5 with Powder Lot # 06-015 (C22C15)	6.34
HVOF SAM2X5 with Powder Lot # 06-015 (C22C16)	8.3
HVOF SAM2X5 with Powder Lot # 06-015 (C22W15)	8.37
HVOF SAM2X5 with Powder Lot # 06-015 (C22W16)	7.43
HVOF SAM2X5 Average	**7.14**
HVOF SAM2X5 Standard Deviation	**0.83**
Metamic Al + B_4C	16.9
Boral Al + B_4C	22.7
Al + B_4C Average	**19.80**

Table IV – Summary of the standard GM9540P Salt Fog Test is summarized here. Note that the salt solution mists (denoted with asterisks) consisted of 1.25% solution containing 0.9% sodium chloride, 0.1% calcium chloride, and 0.25% sodium bicarbonate.

24-Hour Test Cycle for GM9540P Accelerated Corrosion Test		
Shift	Elapsed Time (hrs)	Event
Ambient Soak	0	Salt solution mist for 30 seconds, followed by ambient exposure at 13-28°C (55-82°F)
	1.5	Salt solution mist for 30 seconds, followed by ambient exposure at 13-28°C (55-82°F)
	3	Salt solution mist for 30 seconds, followed by ambient exposure at 13-28°C (55-82°F)
	4.5	Salt solution mist for 30 seconds, followed by ambient exposure at 13-28°C (55-82°F)
Wet Soak	8 to 16	High humidity exposure for 8 hours at 49 ± 0.5°C (120 ± 1°F) and 100% RH, including a 55-minute ramp to wet conditions
Dry Soak	16 to 24	Elevated dry exposure for 8 hours at 60 ± 0.5°C (140 ± 1°F) and less than 30% RH, including a 175-minute ramp to dry conditions

Table V – Composition of standard test media based upon J-13 well water.

Ion	SDW	SCW	SAW
	(mg/L^{-1})	(mg/L^{-1})	(mg/L^{-1})
K^+	34	3,400	3,400
Na^+	409	40,900	40,900
Mg^{2+}	1	1	1,000
Ca^{2+}	1	1	1,000
F^-	14	1,400	0
Cl^-	67	6,700	6,700
NO_3^-	64	6,400	6,400
SO_4^{2-}	167	16,700	16,700
HCO_3^-	947	70,000	0
Si (60°C)	27	27	27
Si (90°C)	49	49	49
pH	8.1	8.1	2.7

FIGURES

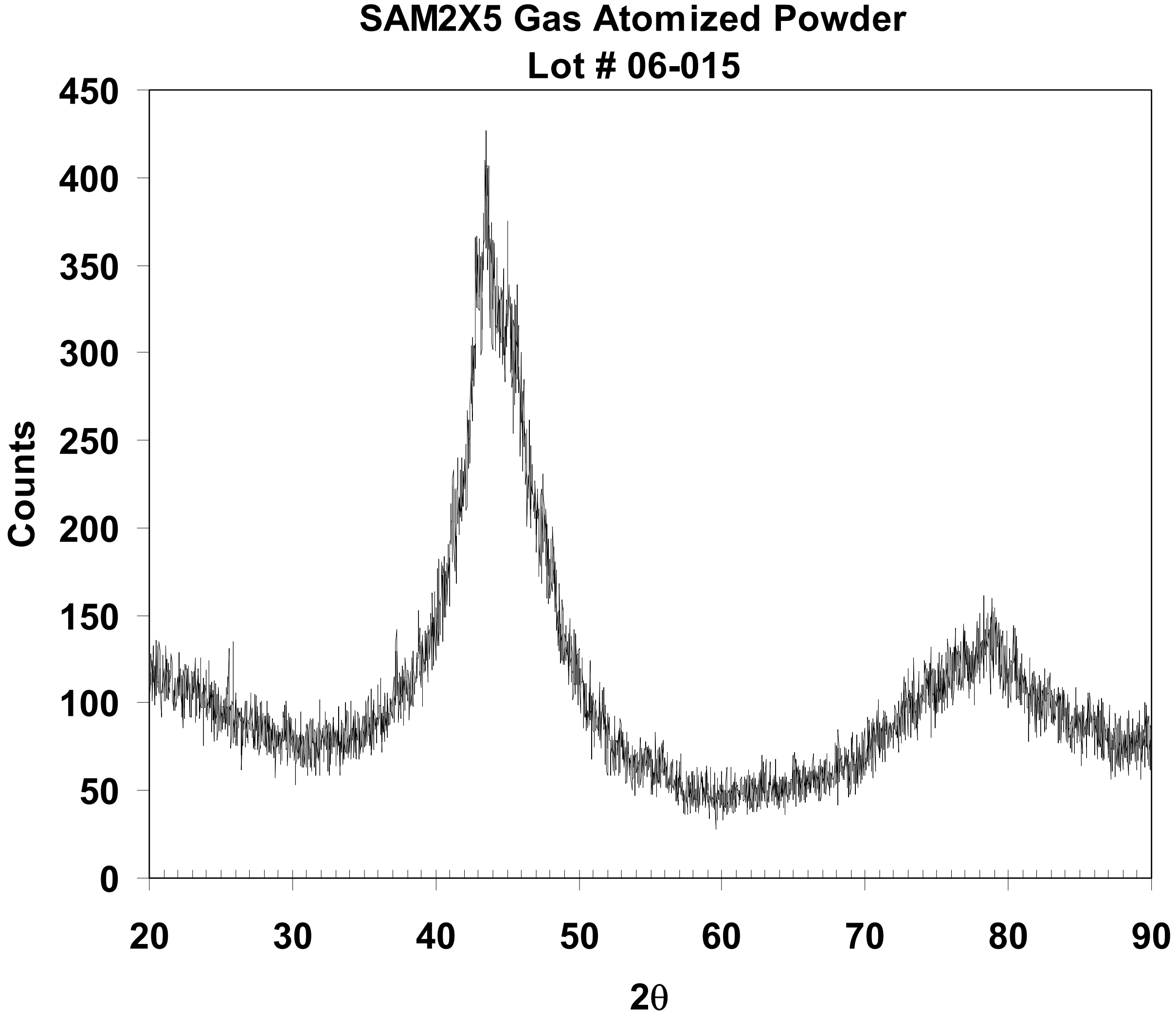

Figure 1 – X-ray diffraction data for SAM2X5 powder identified as Lot # 06-015.

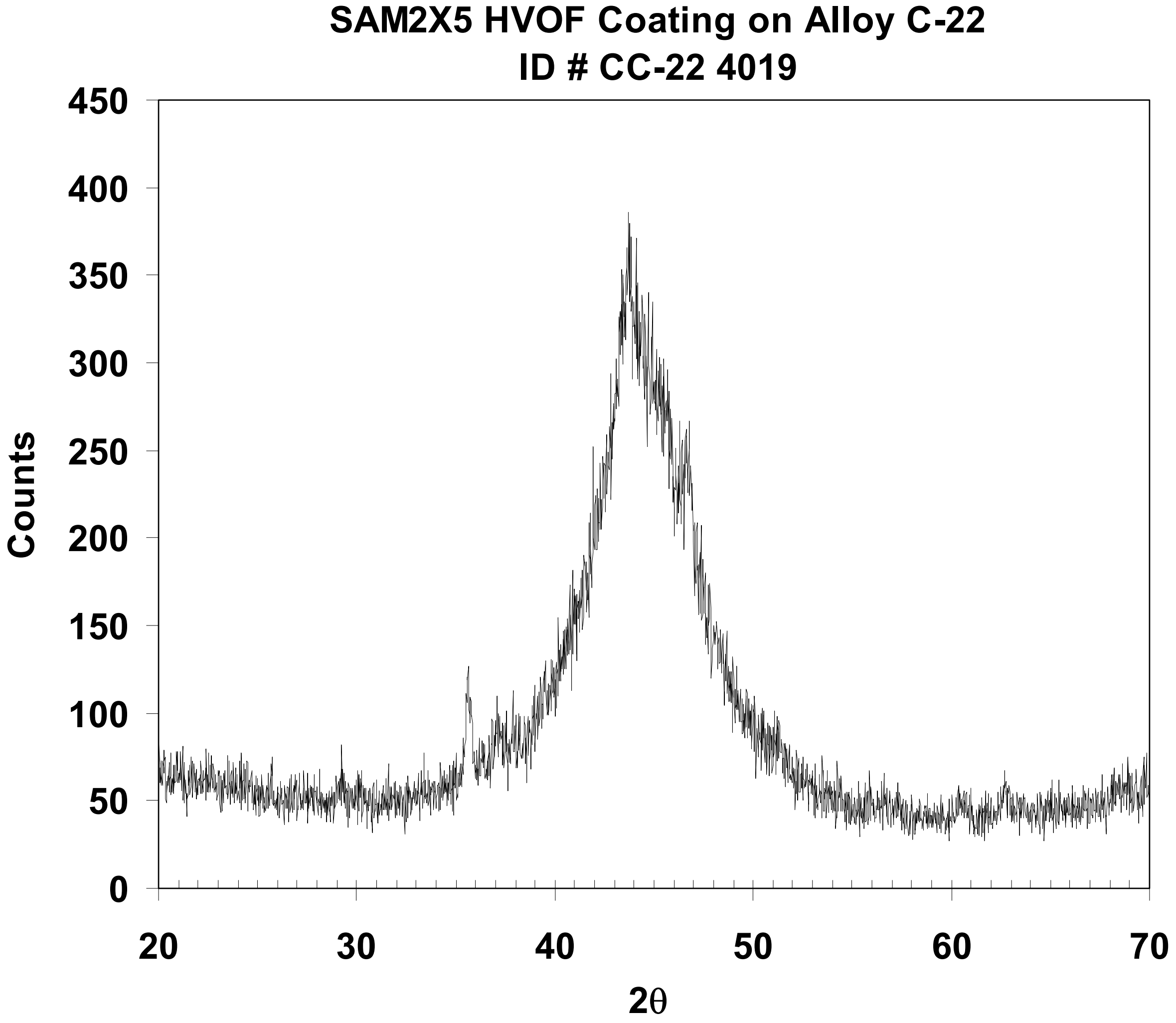

Figure 2 – X-ray diffraction data for SAM2X5 coating, produced with powder identified as Lot # 06-015, and deposited on Alloy C-22 substrate (Sample # CC-22 4019).

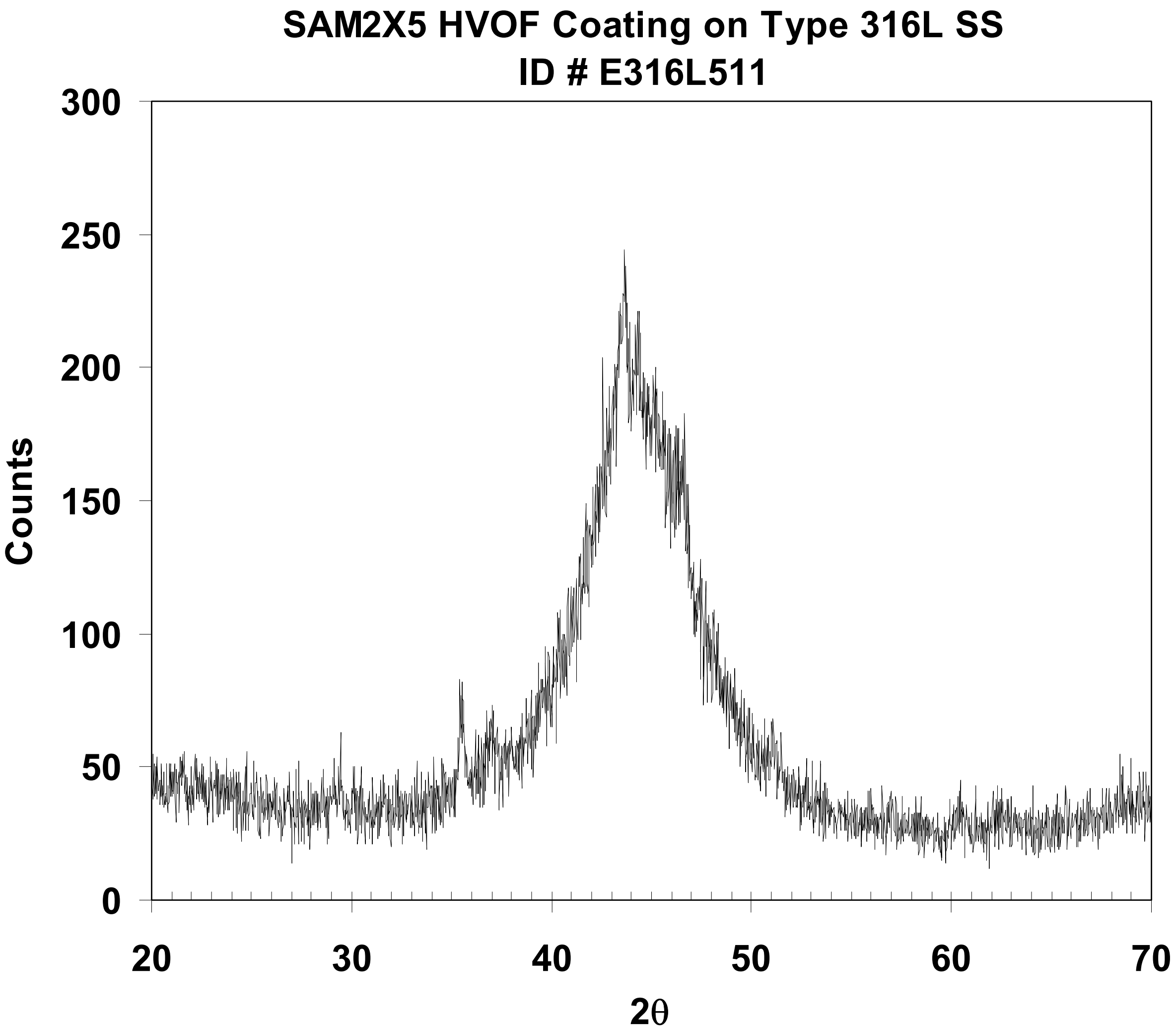

Figure 3 – X-ray diffraction data for SAM2X5 coating, produced with powder identified as Lot # 06-015, and deposited on Type 316L stainless-steel substrate (Sample # E316L511).

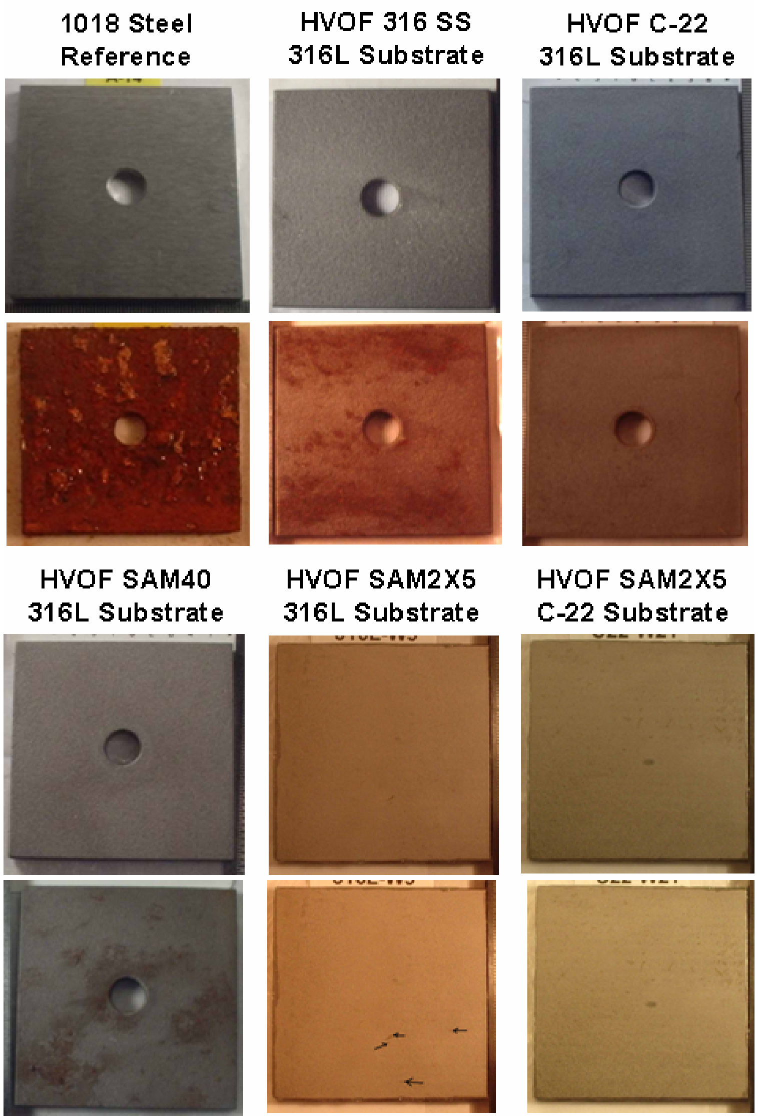

Figure 4 – Various samples before and after eight (8) cycles in salt fog test. Samples # A14, 1018 carbon steel reference specimens; Sample # 316-170, Type 316 stainless-steel coating on 316L substrate; Sample # 316-238, Alloy C-22 coating on 316L substrate; Sample # 316-041, SAM40 coating on 316L substrate; Sample # 316-095, SAM40X3 on 316L substrate; Sample # 316L-W9, SAM2X5 coating 316L substrate; and Sample # C22-W21, SAM2X5 coating on Alloy C-22 substrate. In each case, the top photograph shows the sample before exposure, and the bottom photograph shows the sample afterwards. Arrows were added to the image of the SAM2X5 coating on the 316L substrate to pinpoint small suspected iron oxide spots. In general, the SAM2X5 showed little or no corrosion during salt fog testing.

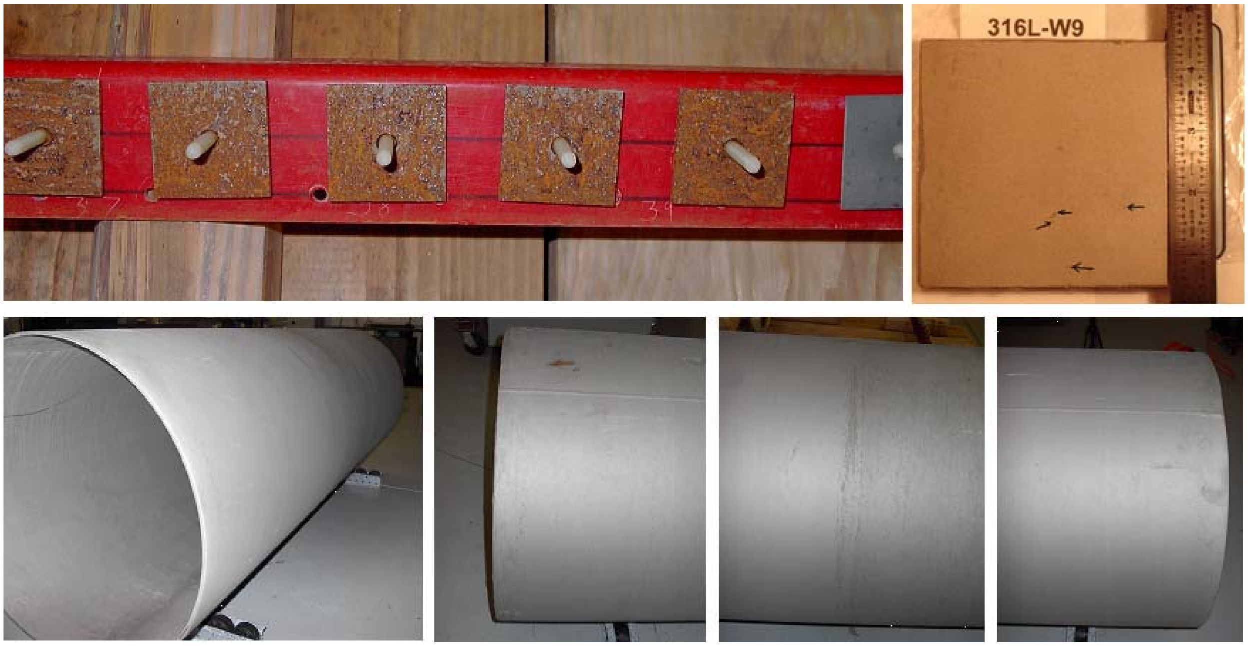

Figure 5 – Samples and prototypes after eight full cycles in the GM salt fog test: (upper left) reference samples of 1018 carbon steel; (upper right) Type 316L stainless steel plate coated with Lot # 06-015 SAM2X5 powder; (lower photographs) half-scale model of spent-nuclear-fuel (SNF) container fabricated from Type 316L stainless steel pipe (Schedule 10s) coated with Lot # 06-015 SAM2X5 powder.

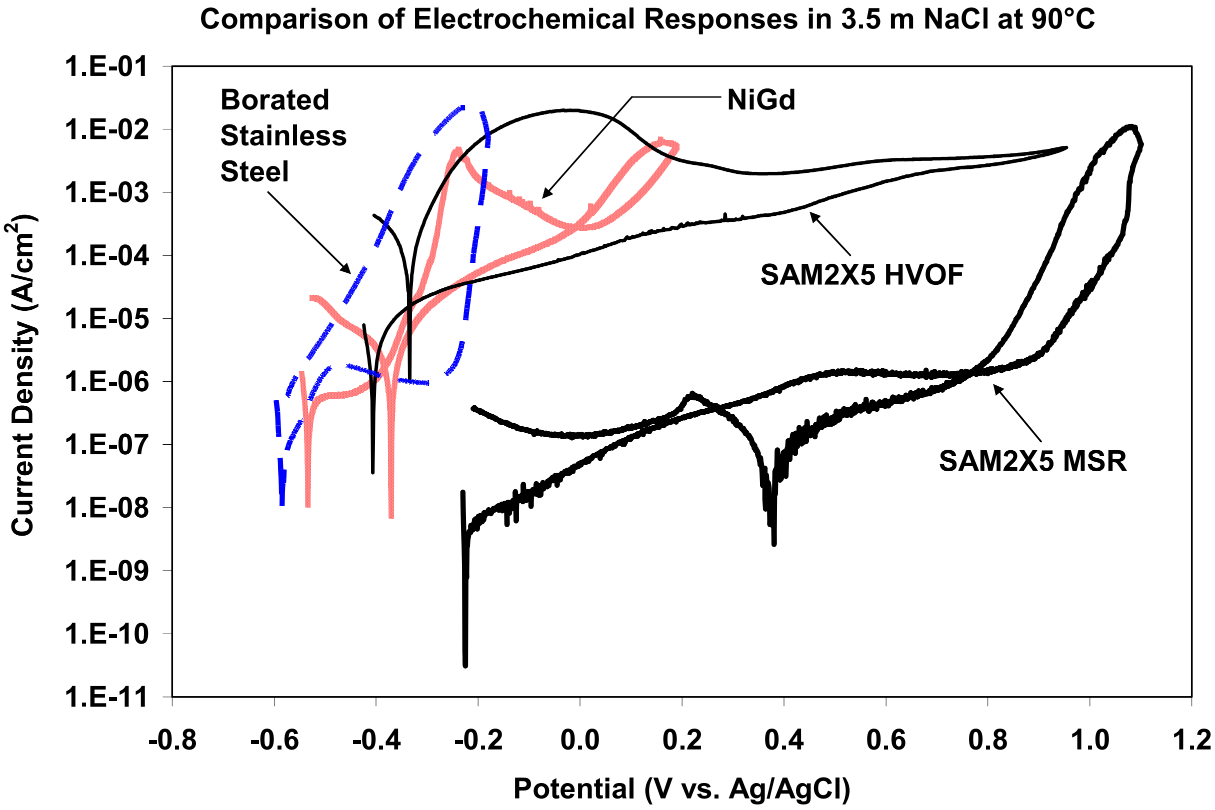

Figure 6 – Cyclic polarization of SAM2X5 melt-spun ribbon, SAM2X5 coating (powder Lot # 06-015), borated stainless steel, and NiGd (Ni-Cr-Mo-Gd) in a 3.5-molal solution of NaCl at 90°C.

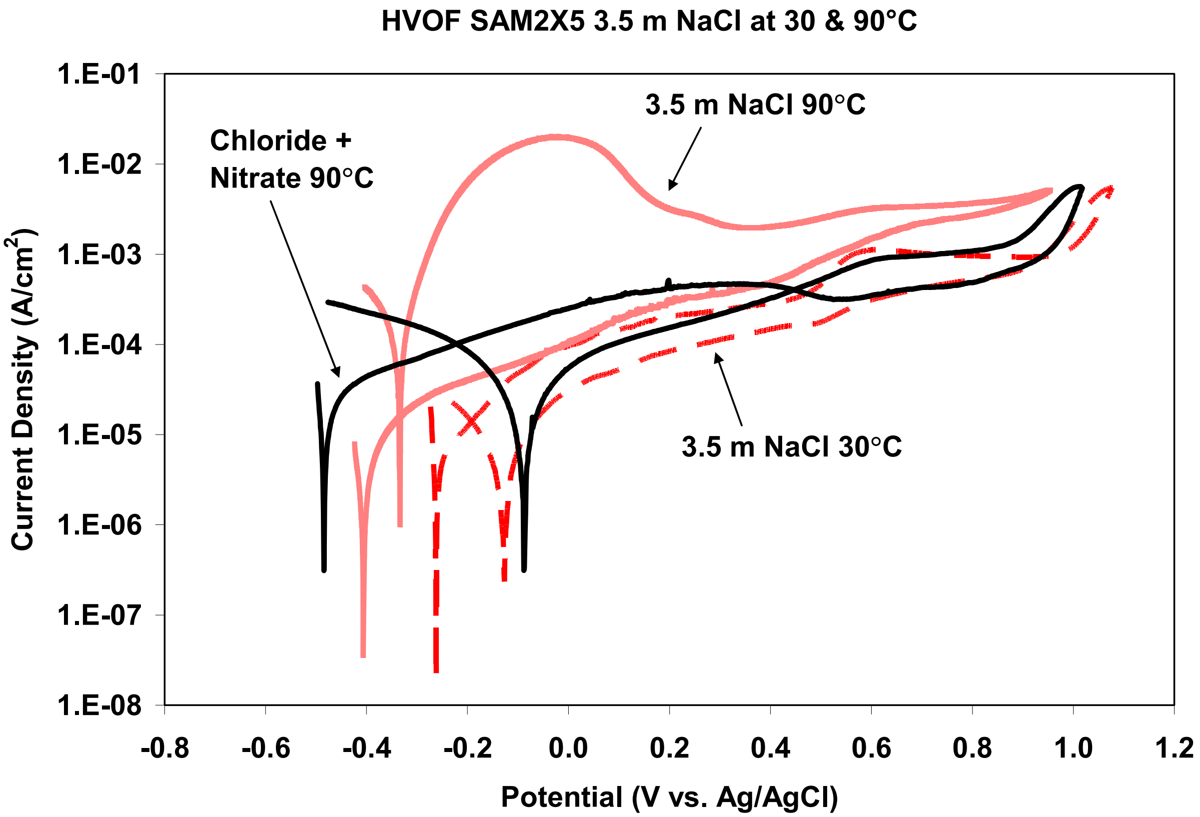

Figure 7 – Cyclic polarization of SAM2X5 coatings on Type 316L stainless steel substrates in a 3.5-molal NaCl solution at 30 and 90°C, as well as 3.5-molal NaCl and 0.525-molal KNO_3 solution at 90°C.

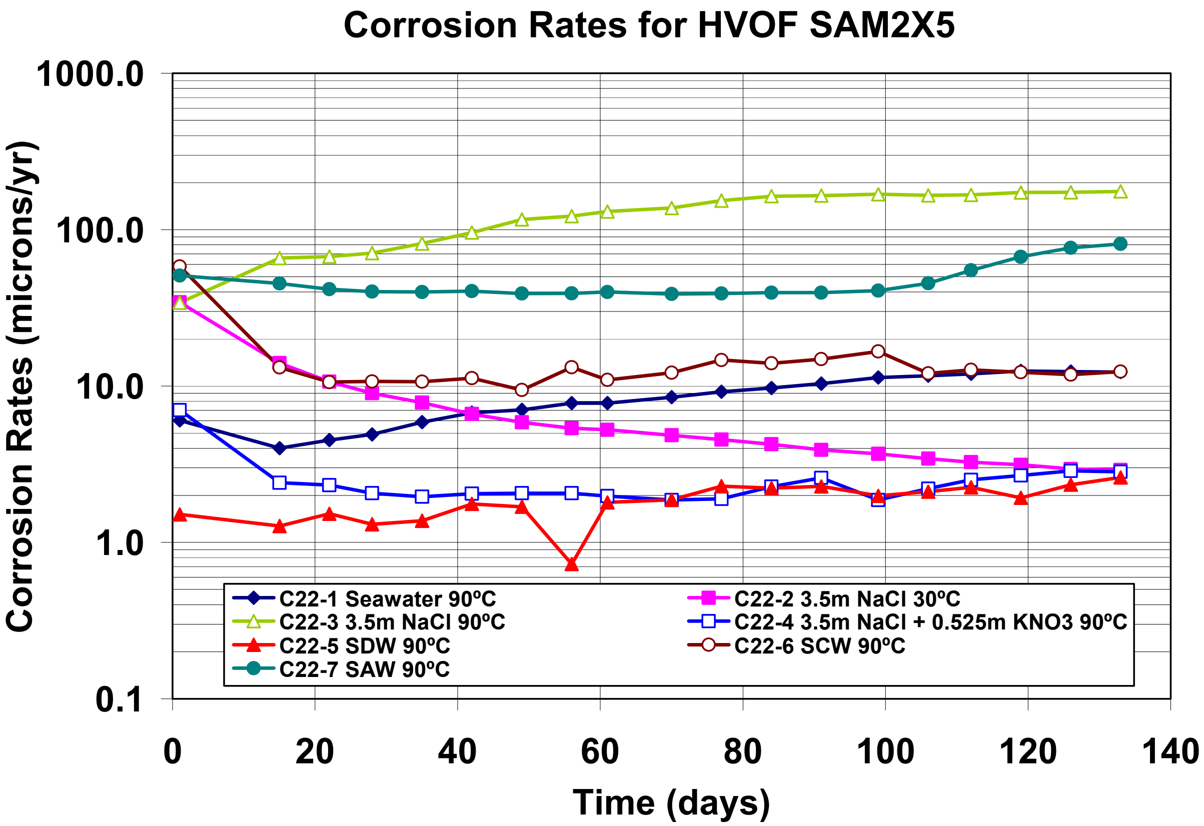

Figure 8 – LPCR values of SAM2X5-coated Alloy C-22 rods during immersion in seven relevant environments over period of approximately 133 days.

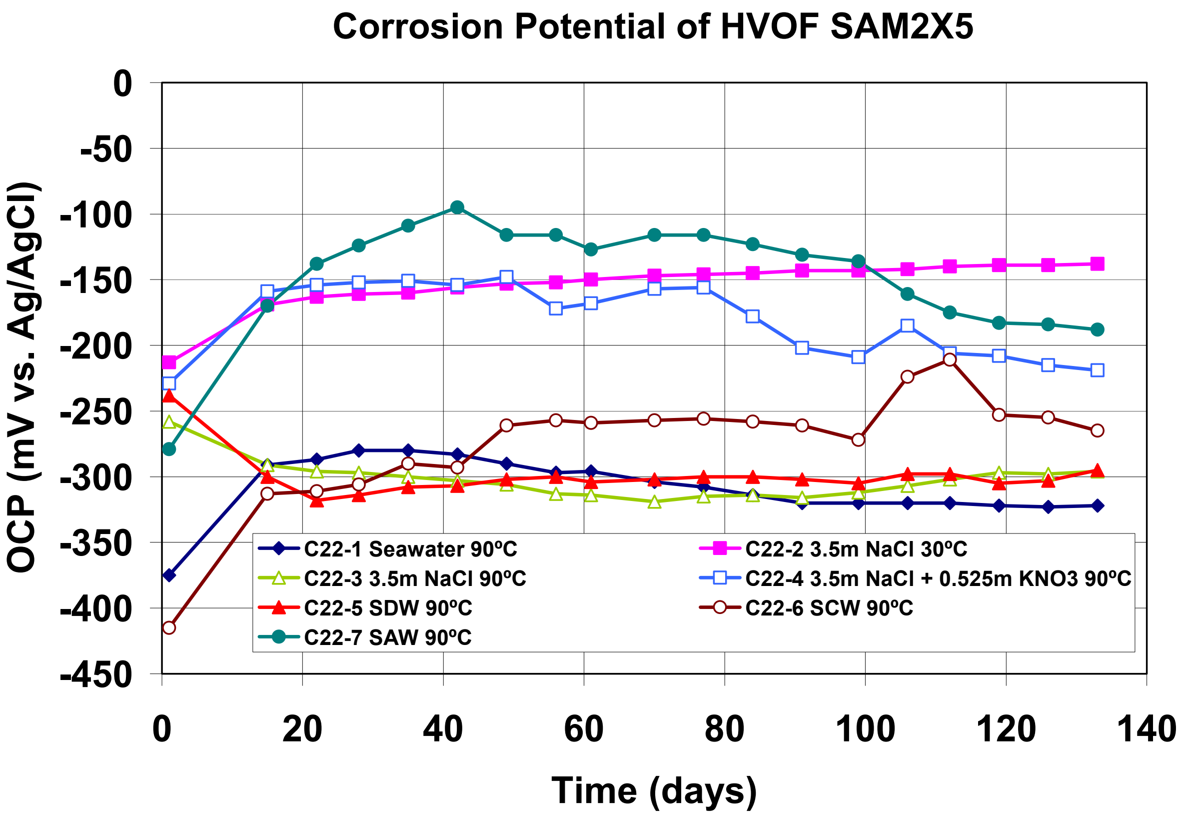

Figure 9 – OCP values of SAM2X5-coated Alloy C-22 rods during immersion in seven relevant environments over period of approximately 133 days.

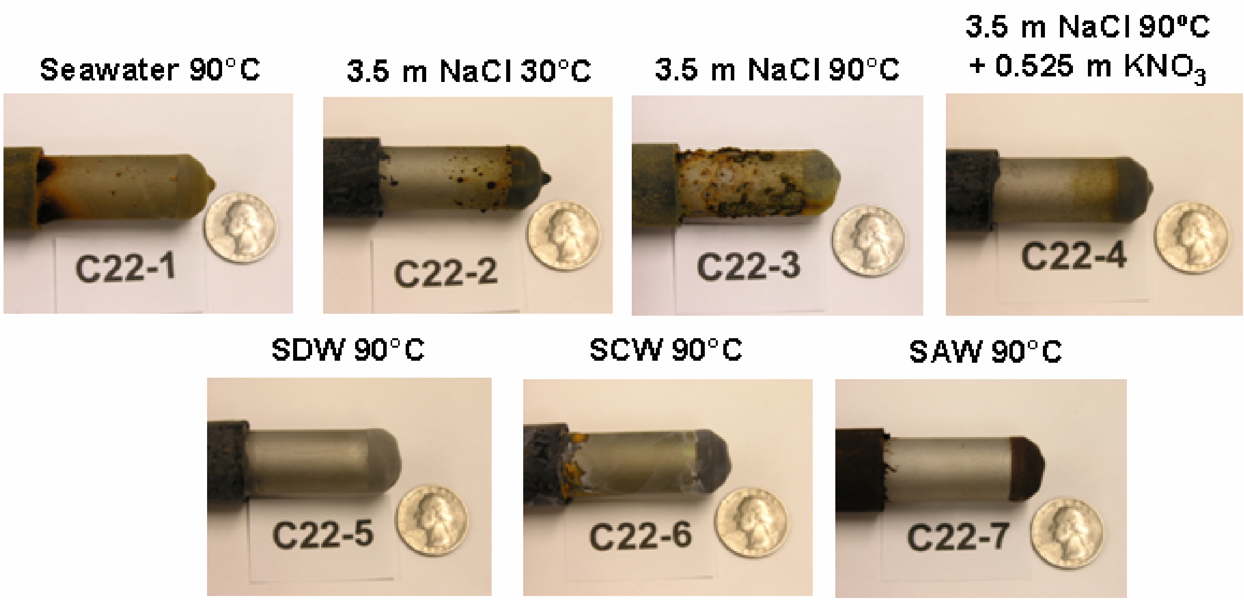

Figure 10 – SAM2X5-coated Alloy C-22 rods used for monitoring OCP and LPCR during immersion testing in seven relevant environments.

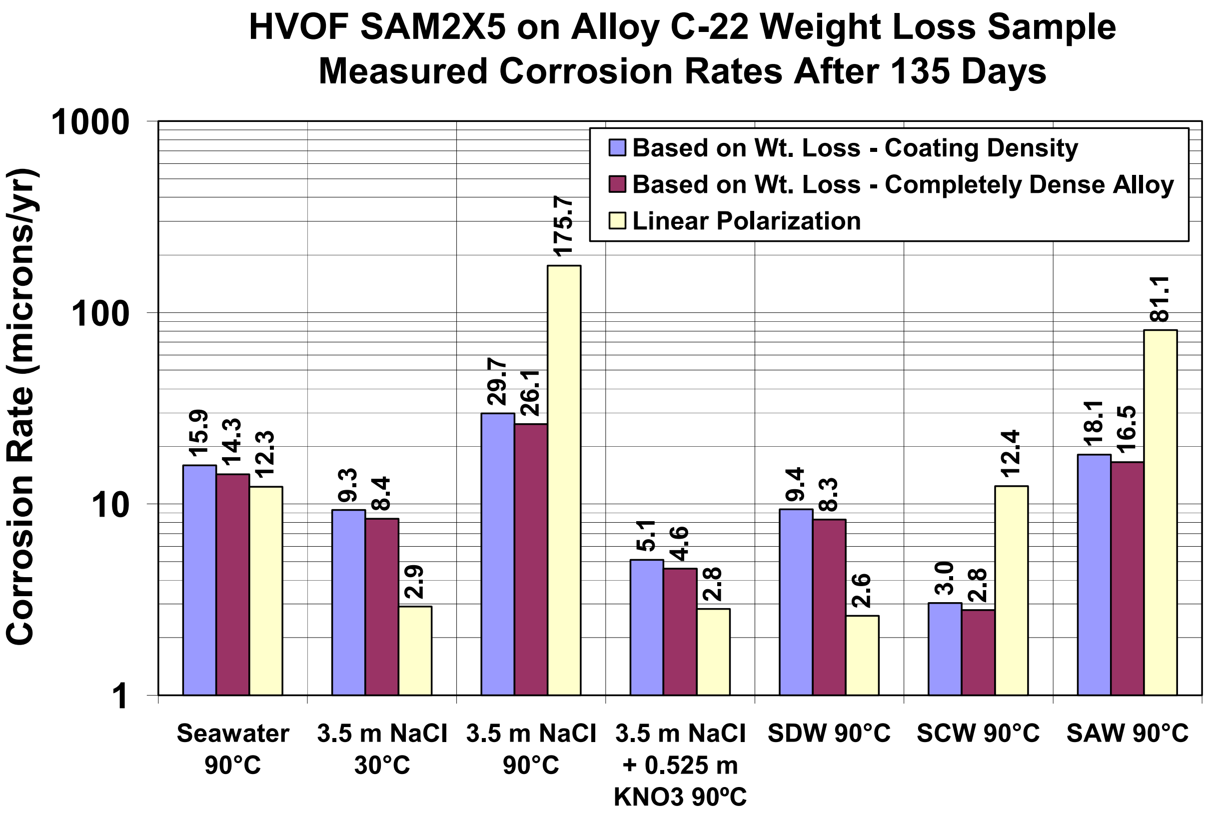

Figure 11 – Corrosion rates determined from weight-loss and dimensional measurements of SAM2X5-coated Alloy C-22 weight-loss samples.

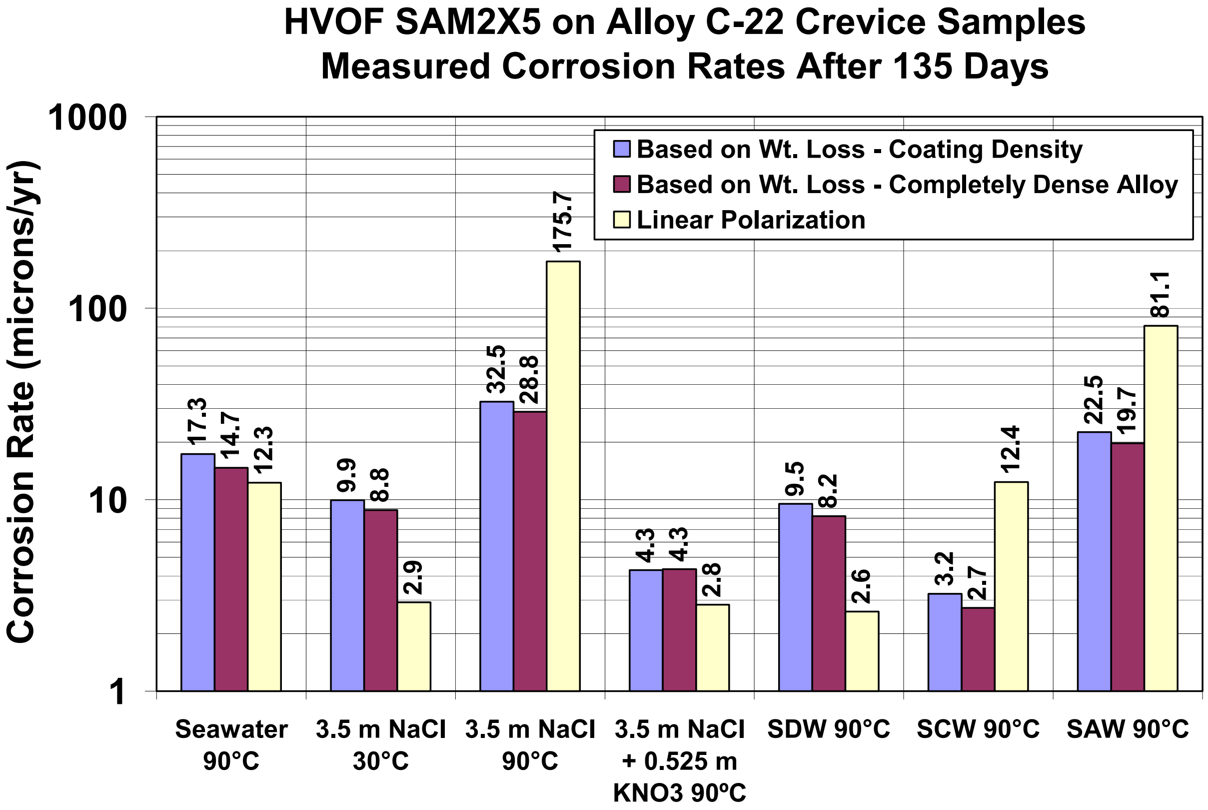

Figure 12 – Corrosion rates determined from weight-loss and dimensional measurements of SAM2X5-coated Alloy C-22 crevice-corrosion samples.

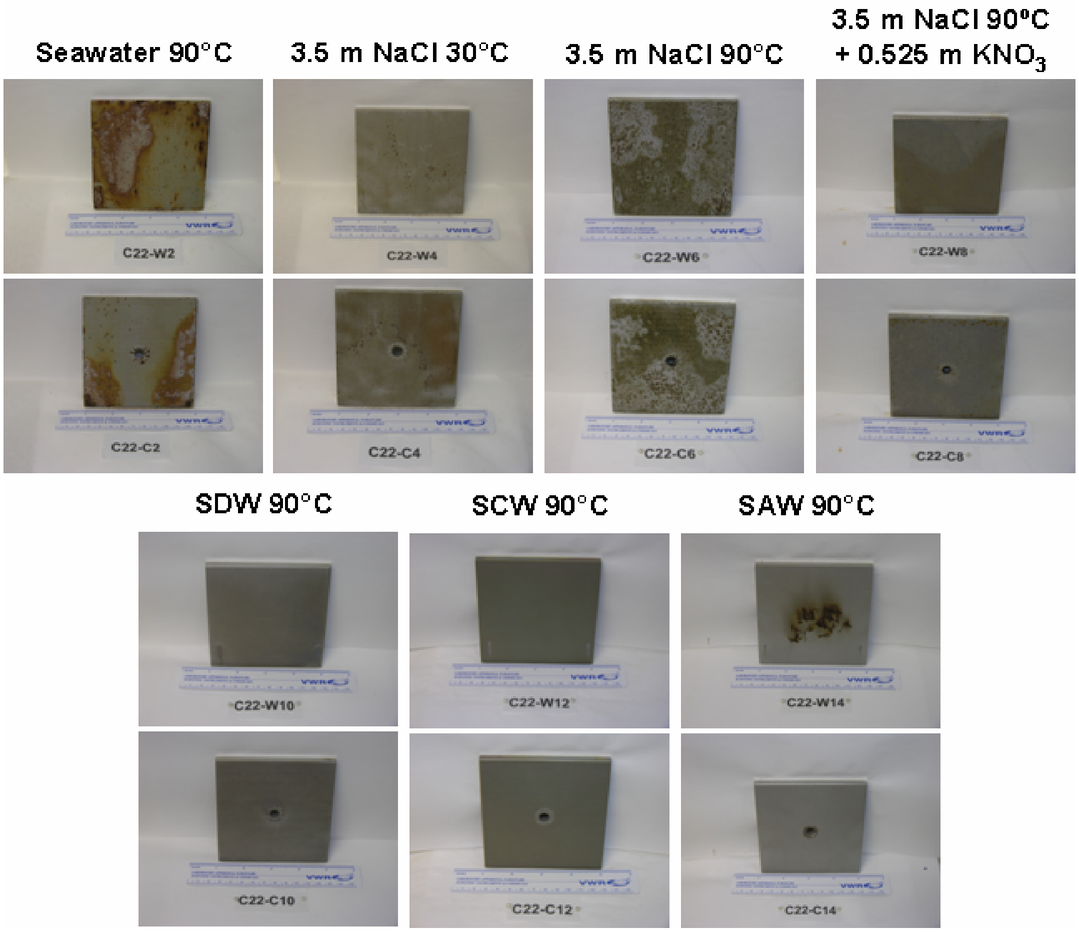

Figure 13 – SAM2X5-coated Alloy C-22 weight-loss samples (identified with C22-W prefix) and crevice samples (identified with C22-C prefix) after immersion testing in seven relevant environments.

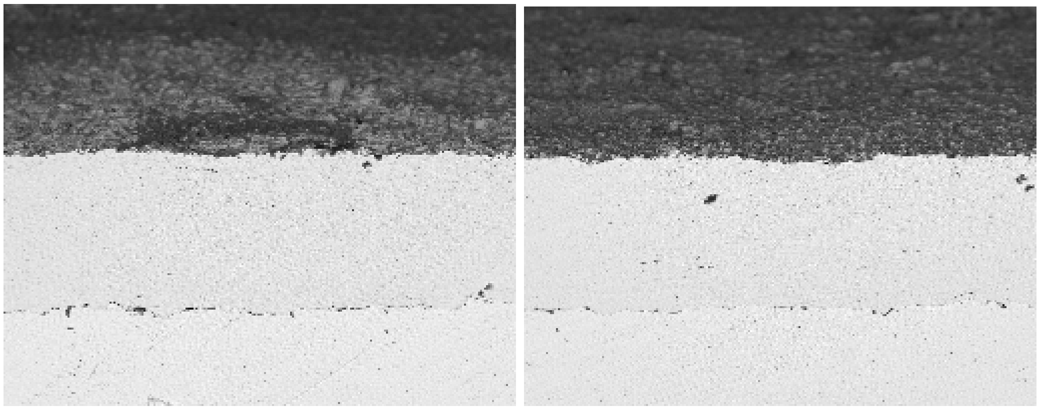

Figure 14 – Backscattered electron image of SAM2X5 sample prepared with Lot # 06-015 powder after 135 days in natural seawater at 90°C. The image on the left shows cross section of superficial spot of iron oxide (left) and the image on the right shows area without corrosion.

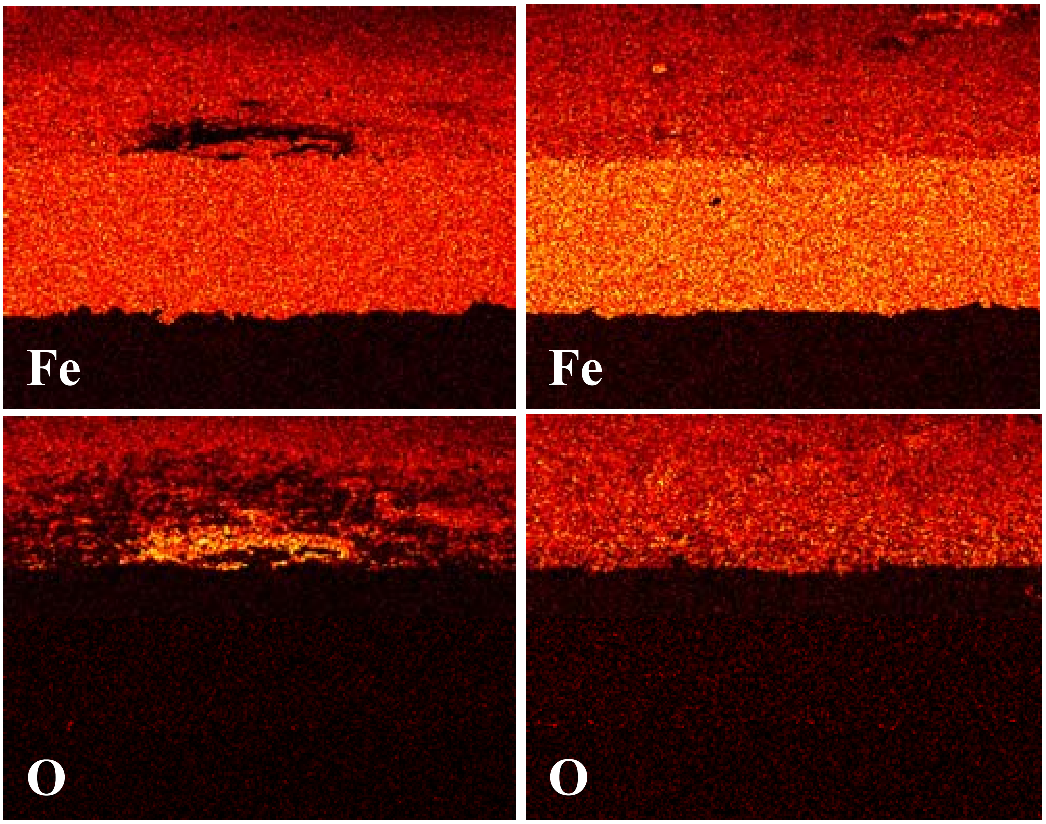

Figure 15 – These images are energy dispersive spectroscopy maps for iron and oxygen corresponding to the backscattered electron images shown in Figure 14. The iron and oxygen maps on the left show a superficial spot of iron oxide, in cross-section, and the iron and oxygen maps on the right show an area of coating, in cross-section, without any corrosion.

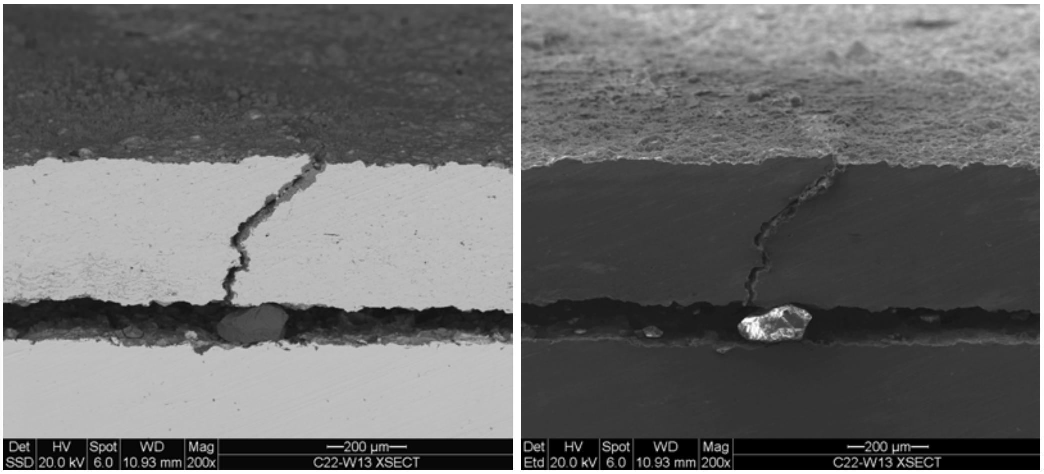

Figure 16 – A backscattered electron image of a SAM2X5 coating sample prepared with Lot # 06-015 powder after 135 days in SAW at 90°C is shown in the left frame, while the corresponding secondary electron image is shown on the right. The aluminum oxide particle responsible for crack initiation is shown at the interface.

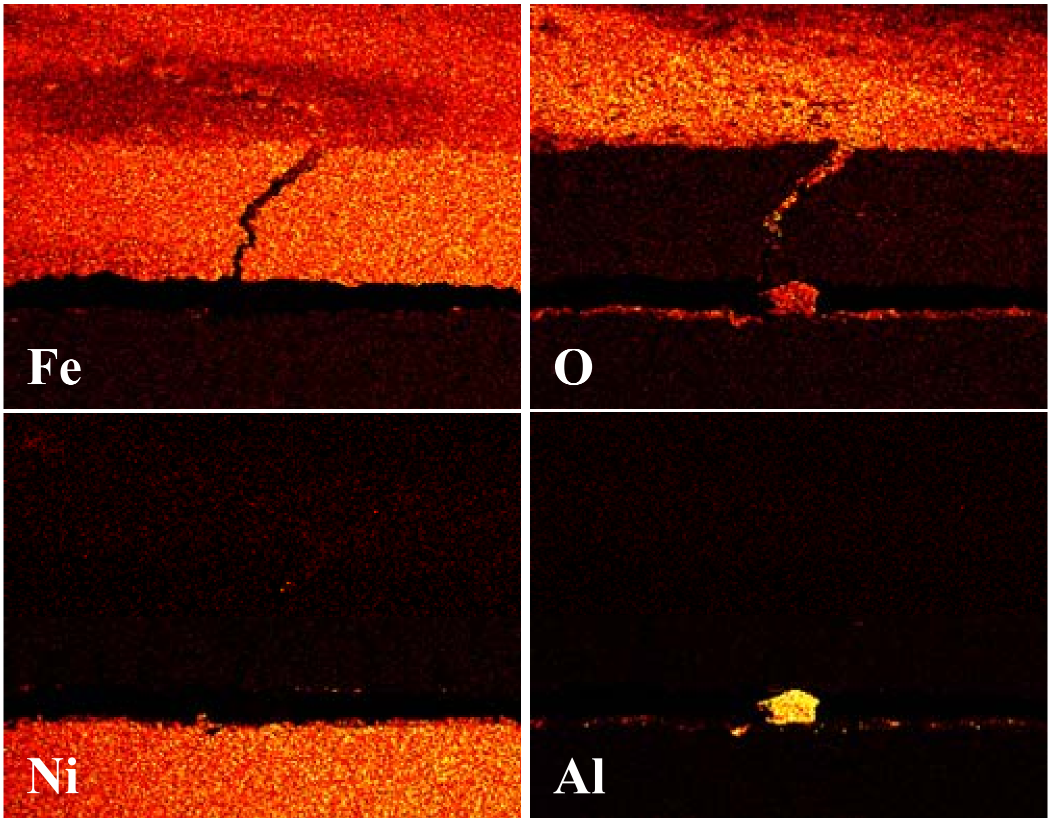

Figure 17 – These images are energy dispersive spectroscopy maps for iron, nickel, oxygen and aluminum corresponding to the backscattered and secondary electron images shown in Figure 16. These data confirm the composition of the particle embedded between the iron-rich coating and the nickel-rich substrate as being aluminum and oxygen rich.